Calcium sulfate veins characterized by ChemCam/Curiosity at Gale crater, Mars

M. Nachon, S. M. Clegg, N. Mangold, S. Schroeder, L. C. Kah, G. Dromart, A. Ollila, J. R. Johnson, D. Z. Oehler, J. C. Bridges, et al.

AGU PUBLICATIONS

JGR

Journal of Geophysical Research: Planets

RESEARCH ARTICLE
10.1002/2013JE004588

Special Section:
Results from the first 360 Sols of the Mars Science Laboratory Mission: Bradbury Landing through Yellowknife Bay

Calcium sulfate veins characterized by ChemCam/Curiosity at Gale crater, Mars

M. Nachon[1], S. M. Clegg[2], N. Mangold[1], S. Schröder[3], L. C. Kah[4], G. Dromart[5], A. Ollila[6], J. R. Johnson[7], D. Z. Oehler[8], J. C. Bridges[9], S. Le Mouélic[1], O. Forni[3], R.C. Wiens[2], R. B. Anderson[10], D. L. Blaney[11], J.F. Bell III[12], B. Clark[13], A. Cousin[2], M. D. Dyar[14], B. Ehlmann[15], C. Fabre[16], O. Gasnault[3], J. Grotzinger[15], J. Lasue[3], E. Lewin[17], R. Léveillé[18], S. McLennan[19], S. Maurice[3], P.-Y. Meslin[3], W. Rapin[3], M. Rice[15], S. W. Squyres[20], K. Stack[15], D. Y. Sumner[21], D. Vaniman[22], and D. Wellington[12]

[1]Laboratoire de Planétologie et Géodynamique de Nantes, CNRS, UMR6112, Université de Nantes, Nantes, France, [2]Los Alamos National Laboratory, Los Alamos, New Mexico, USA, [3]Institut de Recherche en Astrophysique et Planétologie, Toulouse, France, [4]Department of Earth and Planetary Sciences, University of Tennessee, Knoxville, Tennessee, USA, [5]Laboratoire de Géologie de Lyon, Université de Lyon, Lyon, France, [6]Institute of Meteoritics, Department of Earth and Planetary Sciences, University of New Mexico, Albuquerque, New Mexico, USA, [7]Applied Physics Laboratory, Johns Hopkins University, Laurel, Maryland, USA, [8]Jacobs Technology Inc., Johnson Space Center, Houston, Texas, USA, [9]Space Research Centre, Department of Physics and Astronomy, University of Leicester, Leicester, UK, [10]U.S. Geological Survey, Astrogeology Science Center, Flagstaff, Arizona, USA, [11]Jet Propulsion Laboratory, California Institute of Technology, Pasadena, California, USA, [12]School of Earth and Space Exploration, Arizona State University, Tempe, Arizona, USA, [13]Space Science Institute, Boulder, Colorado, USA, [14]Department of Earth and Environment and Department of Astronomy, Mount Holyoke College, South Hadley, Massachusetts, USA, [15]Division of Geological and Planetary Sciences, California Institute of Technology, Pasadena, California, USA, [16]GeoRessources, CNRS, UMR7359, Université de Lorraine, Nancy, France, [17]ISTerre, Université Joseph Fourier, Grenoble, France, [18]Canadian Space Agency, Saint-Hubert, Quebec, Canada, [19]Department of Geosciences, State University of New York at Stony Brook, Stony Brook, New York, USA, [20]Department of Astronomy, Cornell University, Ithaca, New York, USA, [21]Earth and Planetary Sciences, University of California, Davis, California, USA, [22]Planetary Science Institute, Tucson, Arizona, USA

Key Points:
- Calcium sulfate is detected by ChemCam in veins crossing fine-grained sediments
- Veins cross various sediments as a result of postdepositional diagenesis
- Calcium sulfate veins formed through prolonged subsurface fluid circulation

Correspondence to:
M. Nachon,
marion.nachon@univ-nantes.fr

Citation:
Nachon, M. et al. (2014), Calcium sulfate veins characterized by ChemCam/Curiosity at Gale crater, Mars, *J. Geophys. Res. Planets*, *119*, 1991–2016, doi:10.1002/2013JE004588.

Received 29 NOV 2013
Accepted 7 JUL 2014
Accepted article online 12 JUL 2014
Published online 9 SEP 2014

Abstract The Curiosity rover has analyzed abundant light-toned fracture-fill material within the Yellowknife Bay sedimentary deposits. The ChemCam instrument, coupled with Mastcam and ChemCam/Remote Micro Imager images, was able to demonstrate that these fracture fills consist of calcium sulfate veins, many of which appear to be hydrated at a level expected for gypsum and bassanite. Anhydrite is locally present and is found in a location characterized by a nodular texture. An intricate assemblage of veins crosses the sediments, which were likely formed by precipitation from fluids circulating through fractures. The presence of veins throughout the entire ~5 m thick Yellowknife Bay sediments suggests that this process occurred well after sedimentation and cementation/lithification of those sediments. The sulfur-rich fluids may have originated in previously precipitated sulfate-rich layers, either before the deposition of the Sheepbed mudstones or from unrelated units such as the sulfates at the base of Mount Sharp. The occurrence of these veins after the episodes of deposition of fluvial sediments at the surface suggests persistent aqueous activity in relatively nonacidic conditions.

1. Introduction

The Mars Science Laboratory (MSL) Curiosity rover traveled approximately 400 m from the Bradbury landing through the Rocknest region and into Yellowknife Bay (YB) where the entire payload was used to analyze the sediments. During the descent into YB, the landscape transitioned from a regolith-dominated surface into a region dominated by layered sedimentary strata. These outcrops, informally termed the YB formation, reveal a nearly 5 m thick succession of various facies, including conglomerate, sandstone, and mudstone. Mudstone faciès, in particular, were likely deposited in a fluvio-lacustrine environment [*Grotzinger et al.*, 2013]. Light-toned mineral infilling occurs throughout both as vein fills within fractures crosscutting the Yellowknife Bay formation and as infilling of hollow nodules within mudstone faciès [*Grotzinger et al.*, 2013]. ChemCam detected calcium sulfates at the exact location of these veins [*Nachon et al.*, 2013; *McLennan et al.*, 2013], and this finding is critical for interpreting diagenetic processes that may have modified the sediments. After the Opportunity rover found probable calcium sulfate veins at Endeavour Crater [*Squyres et al.*, 2012],

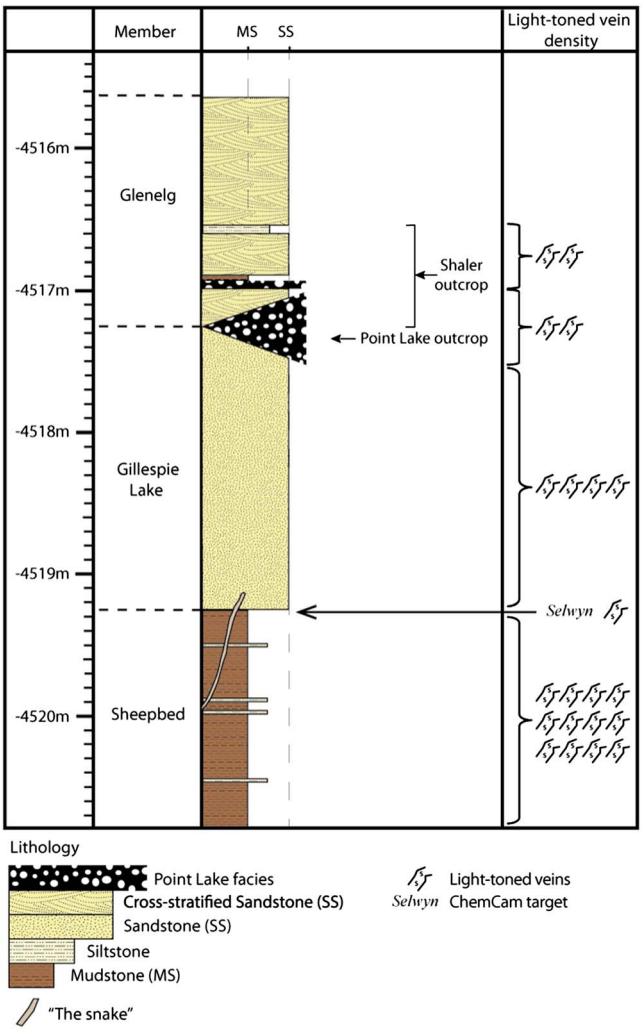

Figure 1. Stratigraphy of the Yellowknife Bay formation as seen along the rover's route. Qualitative estimation of light-toned veins density estimated from ChemCam analyses and MastCam images. The Sheepbed member comprises the highest density of calcium sulfate targets. Adapted from *Grotzinger et al.* [2013].

the presence of similar features inside a different context at Gale crater suggests that such features may provide a greater understanding of aqueous processes across Mars.

This paper examines data from the ChemCam remote Laser Induced Breakdown Spectrometer (LIBS) and Remote Micro-Imager (RMI) [*Maurice et al.*, 2012; *Wiens et al.*, 2012; *Le Mouélic et al.*, 2014] as well as the Mastcam and Mars Hand Lend Imager (MAHLI) imagers to better determine the composition and geological context of these veins. Results are shown in section 3 focusing on the association of sulfur with major and minor elements as well as hydrogen. A quantitative approach also calculates the oxide weight percentage of elements present, allowing an estimation of the stoichiometry. All targets are then analyzed in terms of texture and geological setting in section 4. A discussion pointing toward cross-comparison with other instruments, hydration levels, and implications of these observations is lastly presented in section 5.

2. Approach

2.1. Geological Context

The informal Sheepbed, Gillespie, and Glenelg members comprise the exposed sedimentary strata of the Yellowknife Bay formation. The lowermost units of the Yellowknife Bay formation—the Sheepbed and Gillespie members—are best exposed along the floor and perimeter of YB (Figure 1). The Sheepbed member consists predominantly of mudstone with a few, centimeter-thick, more resistant horizons and forms the exposed floor of Yellowknife Bay. It is overlain along the perimeter of YB by more resistant, laterally continuous sandstone of the Gillespie member [*Grotzinger et al.*, 2013]. By contrast, the overlying Glenelg member consists of a spatially and stratigraphically heterogeneous package of interbedded siltstone, fine- to coarse-grained sandstone (typified by the Shaler outcrop), and possible conglomeratic or diagenetic facies (Point Lake outcrop). The origin of resistant, dark-toned pebbly to vuggy facies of the laterally discontinuous Point Lake facies is not fully understood. Interbedded siltstone and sandstone at the Shaler locality, however, contain distinct channels and compound cross-bedding, which combined with the occurrence of massive coarse sandstone of the Gillespie member suggest deposition within a fluvial system [*Edgar et al.*, 2013]. Clay-rich mudstones of the Sheepbed member similarly suggest shallow lacustrine deposition [*Grotzinger et al.*, 2013; *Vaniman et al.*, 2013].

Light-toned mineral infilling occurs within the Sheepbed, Gillespie, and lower Glenelg members of the YB formation (Figures 1 and 2). The presence of light-toned mineralization is most predominant, however, within mudstone of the Sheepbed member, where it occurs as both vein fill within fractures and infilling of hollow nodules [*Grotzinger et al.*, 2013]. There, veins commonly appear to be more resistant than the surrounding Sheepbed mudstones (Figures 2b and 2c). These occurrences were the most actively documented during the

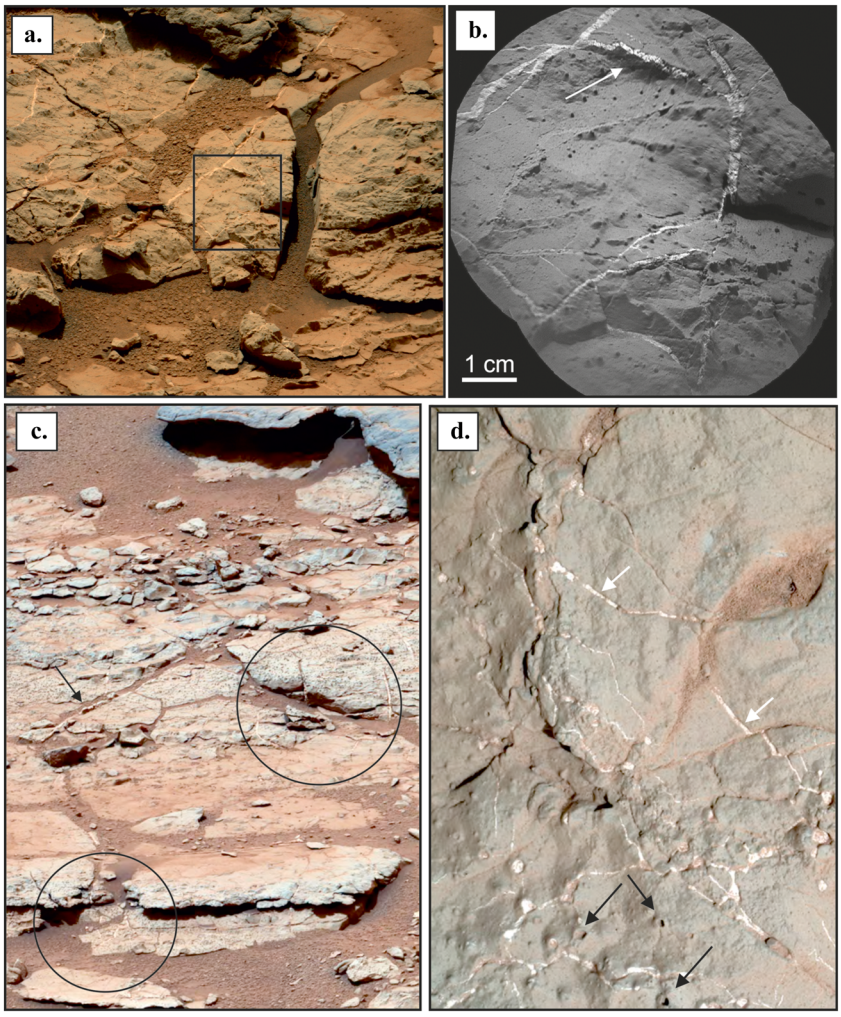

Figure 2. Light-toned veins as observed via Mastcam, ChemCam/RMI, and MAHLI images. (a) Mastcam view of Sheepbed target. The black square shows the (b) RMI close-up. The white arrow points toward a vein protruding from the surrounding mudstone. (c) Mastcam M100 view of the Sheepbed-Gillespie contact (at top) showing a single prominent vein fill (arrow) and several regions where light-toned veins are visible through up to 10 cm of vertical section (circles). Portion of mcam01238 mosaic, sol 297. (d) MAHLI image of the Sheepbed mudstone showing light-toned phases infilling of planar fractures and nodules (white arrows); note that nodules remain unfilled if not intersected by fractures (black arrows), suggesting that mineral-forming fluids were constrained to open fractures.

extensive drilling and sample analysis campaign in the region (sols 125–295). During the whole duration of the YB campaign, veins were intensively targeted by ChemCam laser as reported below.

2.2. Instrument and Method

ChemCam is a suite of instruments consisting of a laser coupled to three spectrometers and an imager, the Remote Micro-Imager (RMI). The Laser-Induced Breakdown Spectrometer (LIBS) allows an elemental analysis of rocks and soils [*Wiens et al*., 2012; *Maurice et al*., 2012] A Nd:KGW laser at the top of the mast is focused through an optical system to target rocks and soils located up to 7 m from the rover. The pits formed by this laser ablation at these distances are typically from 300 to 600 μm in diameter and vary in depth depending on the rheology of the target material and the number of laser shots in the observation. The ChemCam LIBS laser is therefore a microprobe capable of analyzing fine-scale geological features. The laser ablates some material from the sample surface, generating a plasma that contains elementally excited atoms and ions. The excited species emit light as they relax to lower electronic states at discrete wavelengths that are indicative of the elements ablated from the sample. Some of this emission is collected with the telescope and directed into

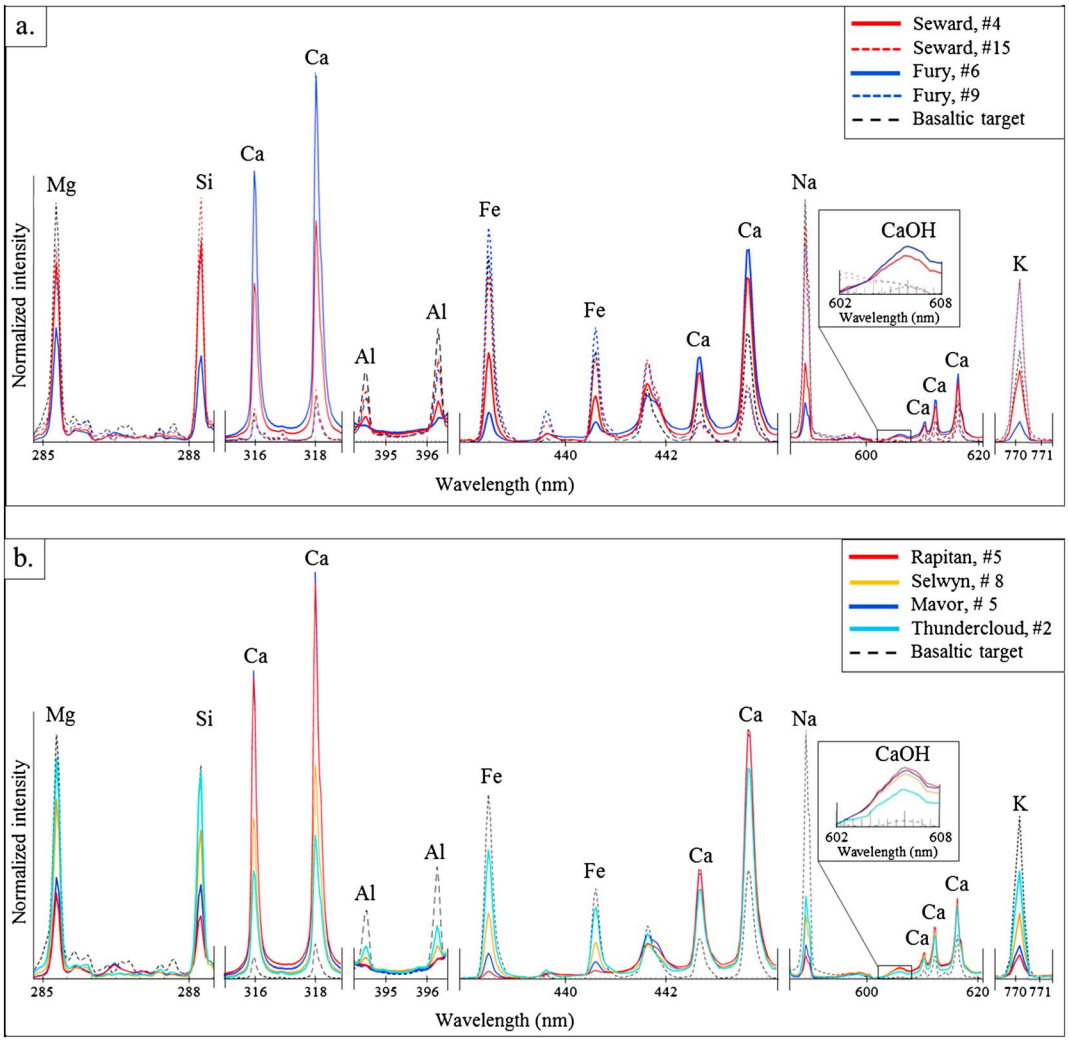

Figure 3. Example of ChemCam targets displaying laser points analysis enhanced in calcium. (a) Point 4 (#4) of the Seward 1 target (full red line) and point 7 of Fury target (full blue line). Dotted red and blue lines correspond to respective surrounding points not enhanced in calcium, for comparison. The ChemCam calibration target in dotted black line (norite target [see *Fabre et al.*, 2011]) is shown for comparison with a classical silicate rock. Seward 1 point 4 and Fury point 7 are depleted in major elements but calcium, compared with surrounding points and the basaltic target. (b) Point 5 of the Rapitan target (red line), point 8 of Selwyn target (orange line), point 5 of Mavor target (dark blue line), point 2 of Thundercloud target (light blue line). For both Figures 3a and 3b, the intensity of the lines is relative to each portion of the spectra.

three spectrometers. The three spectrometers of the ChemCam instrument cover the wavelengths range of 240–900 nm enabling the identification of all major elements [*Wiens et al.*, 2012].

The data of this study were acquired during the daytime, and "dark" spectra (nonlaser background spectra also named passive spectra) were taken after the laser shots in order to remove the contribution due to ambient light. This is especially useful for the hydrogen emission for which the sun has a strong contribution in the form of a relatively deep Frauenhofer absorption line [*Ball et al.*, 2005; *Schröder et al.*, 2013]. Spectra are typically acquired on a number of laser points on each target, using a linescan raster of 5 to 20 points, or a grid of 3 by 3 points, or more. Each point is the result of a burst of typically 30 (sometimes 50) shots, at the same location, with a spectrum acquired for each shot. Deeper depth profiles have also been performed using as many as 600 shots (4 times the maximum of 150 shots in a single laser burst) on a single point. Laser ablation has the advantage of removing the dust with the initial shots and of revealing compositional gradients due to any surface weathering or coatings. The LIBS spectra are preprocessed before elemental compositions are extracted from the spectra. The first 5 shots at each point, which empirically reveal a strong dust contribution, are not taken into average spectra. The latter 25 shots are then averaged to provide a measurement of rock composition (e.g., Figure 3).

Preprocessing includes dark subtraction, denoising, Bremsstrahlung continuum removal, spectral recalibration, the application of an instrument response function that results in an instrument-independent spectrum, and normalization to the total emission of each spectrum, as described by *Wiens et al.* [2013].

The ChemCam spectrometers also were used in passive mode to record visible/near-infrared (400–840 nm) radiance from the Martian surface. Such observations typically were acquired as "darks" by ChemCam after laser shots to assist in calibration of LIBS measurements. *Johnson et al.* [2014] used onboard calibration targets as reflectance standards to reduce the passive radiance observations of sunlit targets to relative reflectance. The spectrometer angular field of view of 0.65 mrad is larger than the ablation cavity, corresponding to ~3–6 mm of diameter depending on distance, compared to $<$0.6 mm for the ablation cavity on rocks [*Wiens et al.*, 2012], and thus, depending on the efficiency of the laser-induced shock wave removing dust [e.g., *Graff et al.*, 2011], these passive spectra may be contaminated by dust.

The RMI provides a panchromatic black and white image and is used to complement the LIBS analysis by providing a visual determination of the exact position of the laser shots. It has a circular field of view of 20 mrad (1.15°) over 1024 × 1024 pixels. According to its pixel angular size of 19.6 μrad/pixel, it can theoretically resolve features as small as 120 microns (2 pixels) for targets located at 3 m from ChemCam [*Le Mouélic et al.*, 2014] and thus provides a critical data set for determining textures. RMI is used hereafter to provide the context of the laser observations in association with wider-angle Mastcam images [*Bell et al.*, 2013].

A systematic search for sulfur lines in spectra and light-toned veins in RMI images was done across the full ChemCam data set. Detections of calcium sulfates reported in this study include all ChemCam data from the first 360 sols (Table 1), comprising ~2100 observations on ~260 separate targets.

3. Elemental Analysis From ChemCam Data

3.1. Qualitative Identification of Calcium Sulfates

ChemCam is able to detect most major elements and most volatiles from the analysis of LIBS spectra. Calcium has many emission lines detectable in the three spectral ranges of the ChemCam spectrometers, for instance, at 316–318 nm, 443–444 nm, and 610–620 nm (Figure 3). Along the rover traverse, several targets have been identified showing especially enhanced calcium lines. It has to be noted that the relationship between peak intensities of a given element and the concentration of this element is not always ideally linear. Matrix effects can result in variations of emission lines unrelated to actual quantitative variations of the element in question, but to optical and mechanical properties of the target. In our study, we normalize the spectra by the total emission intensity (as mentioned in section 2.2) in order to compensate for matrix effects [*Sobron and Wang*, 2011]. Additionally, the Ca peaks enhancement of specific Martian targets is observable over all the spectral ranges, thus corroborating a positive calcium enrichment in these targets. Moreover, in addition to atomic Ca emissions, Ca molecular bands have been observed: at 552.3 nm (belonging to the green system of the CaO molecule [*Forni et al.*, 2014]) and near 606 nm (Figure 3), interpreted as the CaOH band [*Gottfried et al.*, 2009]). It is considered that high concentrations of the elements composing the molecules must be present for molecular emissions to be observed [*Cremers and Radziemski*, 2006].

Figure 3 details these observations for the targets Seward 1 (sol 187), Fury (sol 188), Rapitan (sol 135), Selwyn (sol 154), Mavor (sol 160), and Thundercloud (sol 166). Point 4 of Seward 1 (full red line) and point 6 of Fury (full blue line) display Ca lines higher than those from respective surrounding points (dotted red and blue lines), in all three spectral ranges; moreover, they are characterized by a depletion in other major elements, as exemplified for the selected Si, Al, Na, Fe, Mg, and K lines (Figure 3a). Like the points in Figure 3b, their spectra are also totally distinct from that of the ChemCam calibration target (dotted black line) [*Fabre et al.*, 2011] of known basaltic composition. Calcium-rich points are depleted in Si compared to the surrounding points, suggesting the predominance of a nonsilicate phase associated with Ca.

Our detailed investigation has also provided evidence for sulfur lines, an element usually difficult to identify using LIBS data. Indeed, electronically excited sulfur in the plasma of sulfur-bearing samples are shown to react with oxygen in laboratory atmosphere, limiting detection of sulfur, at least in terrestrial atmosphere [*Dudragne et al.*, 1998]. However, accurate detection of sulfur can nevertheless be achieved in a Mars atmosphere better than in the Earth's atmosphere [*Sallé et al.*, 2004; *Sobron et al.*, 2012]. Many LIBS researchers use the stronger sulfur lines S (I) present in the UV range (125–180 nm) or in the near-infrared ($>$920 nm) [e.g. *Dudragne et al.*, 1998], which are

Table 1. ChemCam Calcium Sulfate Targets Identified During the First 360 Sols of the Rover Traverse[a]

Sol Number	Target Name	Point of Target	Sulfur Detection	High Ca Lines	Hydrogen Detection	RMI Interpretation	Stratigraphy
113	Bell Island 1	1	X	X	X	Vein	Point Lake
125	Crest	1	X	X	X	Vein	Gillespie
		9	X	X	X		
130	Richardson 2	1	X	X	X	Vein?	Sheepbed
		2	X	X	X		
		4	X	X	X		
132	Gillespie Lake 2	3	X	X	X	Bowl	Gillespie
135	Rapitan	1	X	X	X	Nodular texture	Sheepbed
		2	X	X	X		
		4	X	X	X		
		5	X	X	X		
		6	X	X	X		
		7[b]		X	X		
		8	X	X	X		
		9	X	X	X		
150	Hayhook	4[b]		X	X	Vein?	Sheepbed
151	Quartet	7	X	X	X	Vein	Sheepbed
152	Quartet new	7	X	X	X	Vein	Sheepbed
154	Selwyn	8[b]	X	X		Nodular texture	Sheepbed/Gillespie
157	Selwyn 1	14	X	X	X	Nodular texture	Sheepbed/Gillespie
		15[b]		X			
157	Selwyn 2	3	X	X	X		
		5[b]		X			
159	Selwyn 3	1[b]		X	0	Nodular texture	Sheepbed/Gillespie
160	Mavor	5	X	X	X	Nodule/Nodular texture	Sheepbed
		6	X	X	X		
165	John Klein RP3	7[b]		X	X	Vein	Sheepbed
165	Tukarak	2	X	X	X	Vein	Sheepbed
		4	X	X	X		
		7	X	X	X		
166	Thundercloud	2	X	X	X	Nodules/Vein	Sheepbed
187	Seward 1	4[b]	X	X		Vein	Sheepbed
		5	X	X	X		Sheepbed
188	Kazan	6	X	X	X	Nodule	Sheepbed
188	Fury	6	X	X	X	Vein	Sheepbed
227	Drillhole	7[b]	X	X		Vein	Sheepbed
		9	X	X	X		
232	Ruth	11	X	X	X	Vein/Nodule	Sheepbed
		12	X	X	X	Vein/Nodule	Sheepbed
		18	X	X	X	Vein/Bowl	Sheepbed
		23	X	X	X	Bowl	Sheepbed
		24	X	X	X	Bowl	Sheepbed
271	Narrows3 CCAM Target	1	X	X	X	Nodule/Vein	Sheepbed
275	Cumberland Bowl	3	X	X	X	Bowl/vein	Sheepbed
275	Cumberland 3	1[b]		X	X	Vein/Nodules	Sheepbed
		3	X	X	X		
		9	X	X	X		
292	Cumberland 3 ccam	2	X	X	X	Bowl/Vein	Sheepbed
298	Cape Strawberry	9[b]		X	X	Vein	Sheepbed
305	Measles Point	9	X	X	X	Nodule	Point Lake
316	Reddick Bight	3	X	X	X	Vein	Shaler
		5	X	X	X		
		6[b]		X	X		
		8	X	X	X		
317	Denault	4	X	X	X	Vein	Shaler

[a]The "point of target" column indicates the analysis positions, within the laser raster of each target. The calcium column refers to locations where calcium emission lines are higher than those of the others points of the same target.

[b]Putative (sulfur or hydrogen) detection.

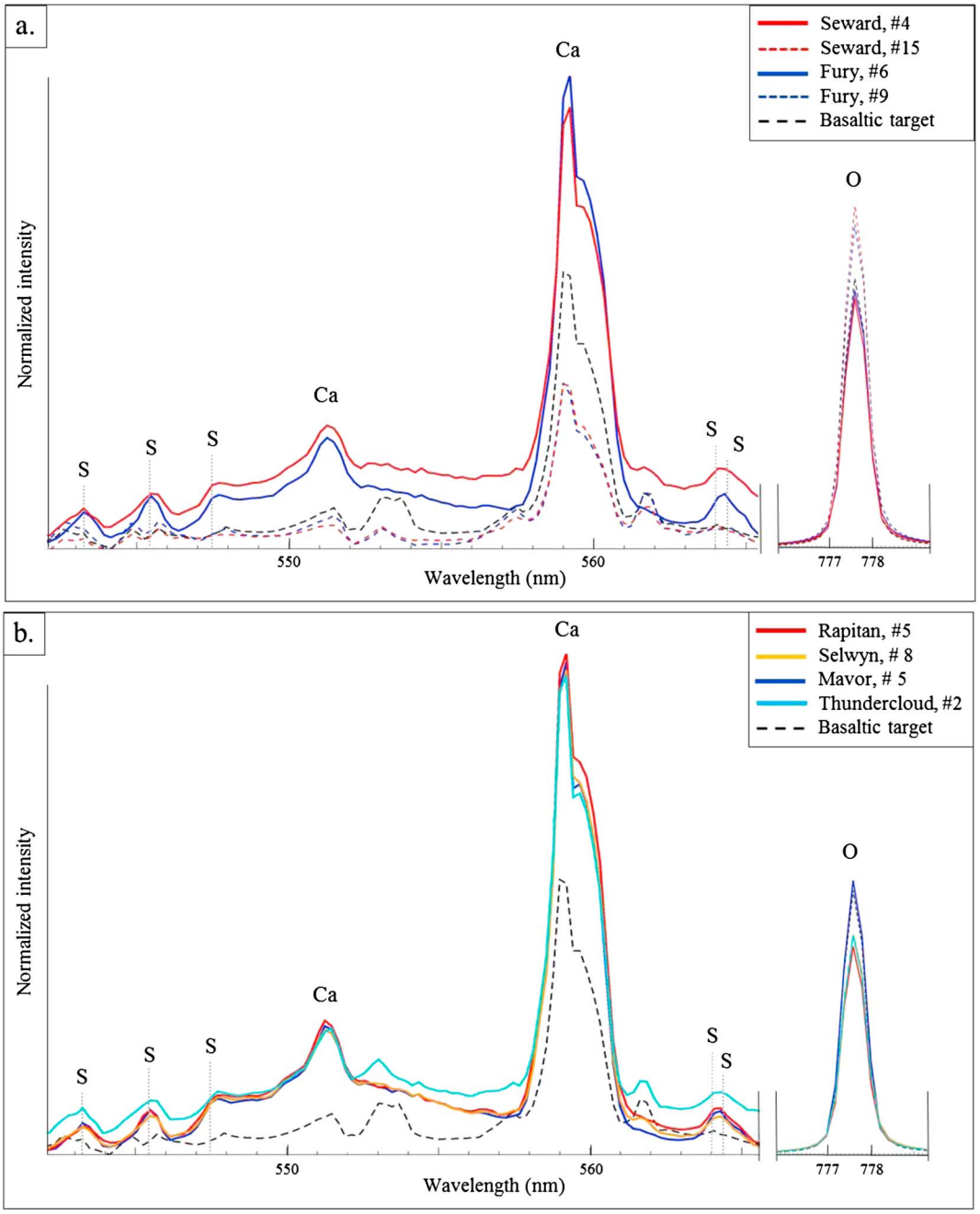

Figure 4. (a and b) Sulfur and oxygen detection from ChemCam spectra. The sulfur peaks indicated (dashed gray lines) were identified in laboratory data [e.g., *Dyar et al*., 2011]. For both Figures 4a and 4b, the intensity of the lines is relative to each portion of the spectra.

both out of the ChemCam spectral range. Weaker sulfur lines S (II) have been identified in laboratory in the visible range, namely, a triplet at wavelengths of 543.3, 545.4, and 547.4 nm and a doublet at 564.0 and 564.4 nm [*Sallé et al*., 2004; *Dyar et al*., 2011; *Sobron and Wang*, 2011; *Sobron et al*., 2012; *Cousin et al*., 2011]. Most of the S lines in this spectral range, however, overlap with other emission lines of major elements (such as Fe, where present) which are notably stronger, limiting the possible identifications except for relatively pure sulfur-bearing minerals (sulfates, sulfides, etc.). The presence of oxygen is a strong indicator that the material observed is oxidized contrary to sulfides. The strong depletion of other elements besides calcium and oxygen within spectra of targets such as Seward 1, Fury, Rapitan, Selwyn, Mavor, and Thundercloud allows us to identify the abovementioned lines in these targets (Figure 4). Results show that one or more relatively pure S-bearing phases

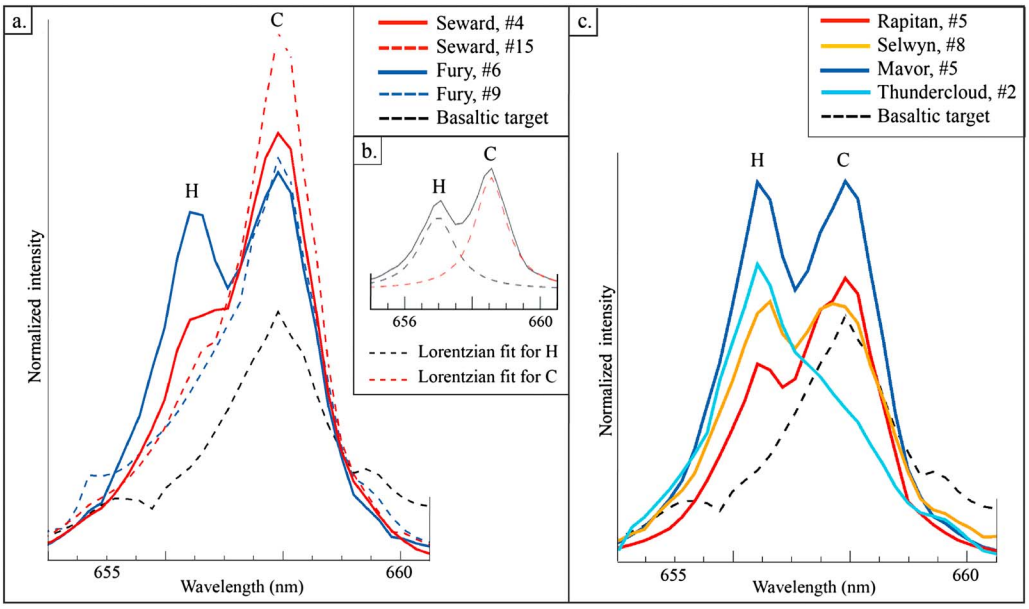

Figure 5. (a and c) Variation of the hydrogen emission line among calcium sulfates as seen by ChemCam, suggesting variability in hydration. Note that the C is a contribution of the atmospheric CO_2, which apparent increase is only a consequence of the presence of H. (b) Lorentzian fits of the hydrogen and carbon lines, to illustrate the overlap.

were hit by the laser (full lines). By contrast, spectra of the same targets, but from points outside the Ca-rich points, do not show any S lines (Figure 4a), indicating a strong correlation between locations with enriched Ca and those with S.

Other elements that may serve as anions linked to Ca have been systematically searched for. The C lines present at 247 and 658 nm are present in all spectra and reflect a contribution from atmospheric CO_2 [e.g., *Ollila et al.*, 2011]. The C emission line at 658 nm is on the shoulder of the hydrogen line (Figure 5b), and rises in intensity with the increase of H, but not as a result of an augmentation in C content [*Schröder et al.*, 2013]. No specific spectral signatures were identified for C that could indicate significant amount of carbonates. A few high-calcium phases at Rocknest (sols 60 to 100), especially location 5 in the Epworth soil [*Clegg et al.*, 2013] have possible phosphorus and fluorine, suggesting the presence of fluoroapatite [*Forni et al.*, 2014]. These peaks are not detected in the sulfur-rich targets of the YB area. Chlorine is difficult to detect with LIBS except in relatively high abundances (above 5–10%) [e.g., *Sallé et al.*, 2004]. CaCl molecular band has been detected within targets identified as calcium sulfates [*Forni et al.*, 2014]: Crest (point 9, sol 125), Measles Point (point 9, sol 305), and Cumberland3 ccam (point 2, sol 292). As Na signature is also present, this could suggest the presence of NaCl within these targets. Note that Cl is recombined with Ca in the plasma, but was not necessarily bound with Ca before. Thus, the identification of enhanced Ca and S lines in concert, without other significant contributions but oxygen, points toward the presence of calcium sulfates.

Systematic analyses of spectra have been made for all targets encountered at Yellowknife Bay. Table 1 summarizes all points that have enhanced Ca with the presence of S in concert. In a few targets, sulfur is only tentatively detected; those targets correspond to relatively limited calcium enrichment, suggesting a stronger mixing with the surrounding rock. The majority of the targets presented have been analyzed at similar distances (2.8 m ± 0.5) from ChemCam, thus limiting variations due to this parameter. A more quantitative estimate of the detected elements is done in section 3.3.

3.2. Hydration State of Calcium Sulfates

Calcium sulfates occur as a nonhydrated phase (anhydrite, $CaSO_4$) or as one of two hydrated phases (bassanite, $CaSO_4.1/2H_2O$, which can contain a somewhat variable water content, and gypsum, $CaSO_4.2H_2O$). ChemCam identifies the presence of hydrogen at 656 nm, as already found in soils and dust [*Meslin et al.*, 2013] and within fluvial conglomerates [*Williams et al.*, 2013]. However, the quantification of H is strongly affected by matrix effects [*Schröder et al.*, 2013], thus making difficult the discrimination between bassanite and gypsum. Matrix

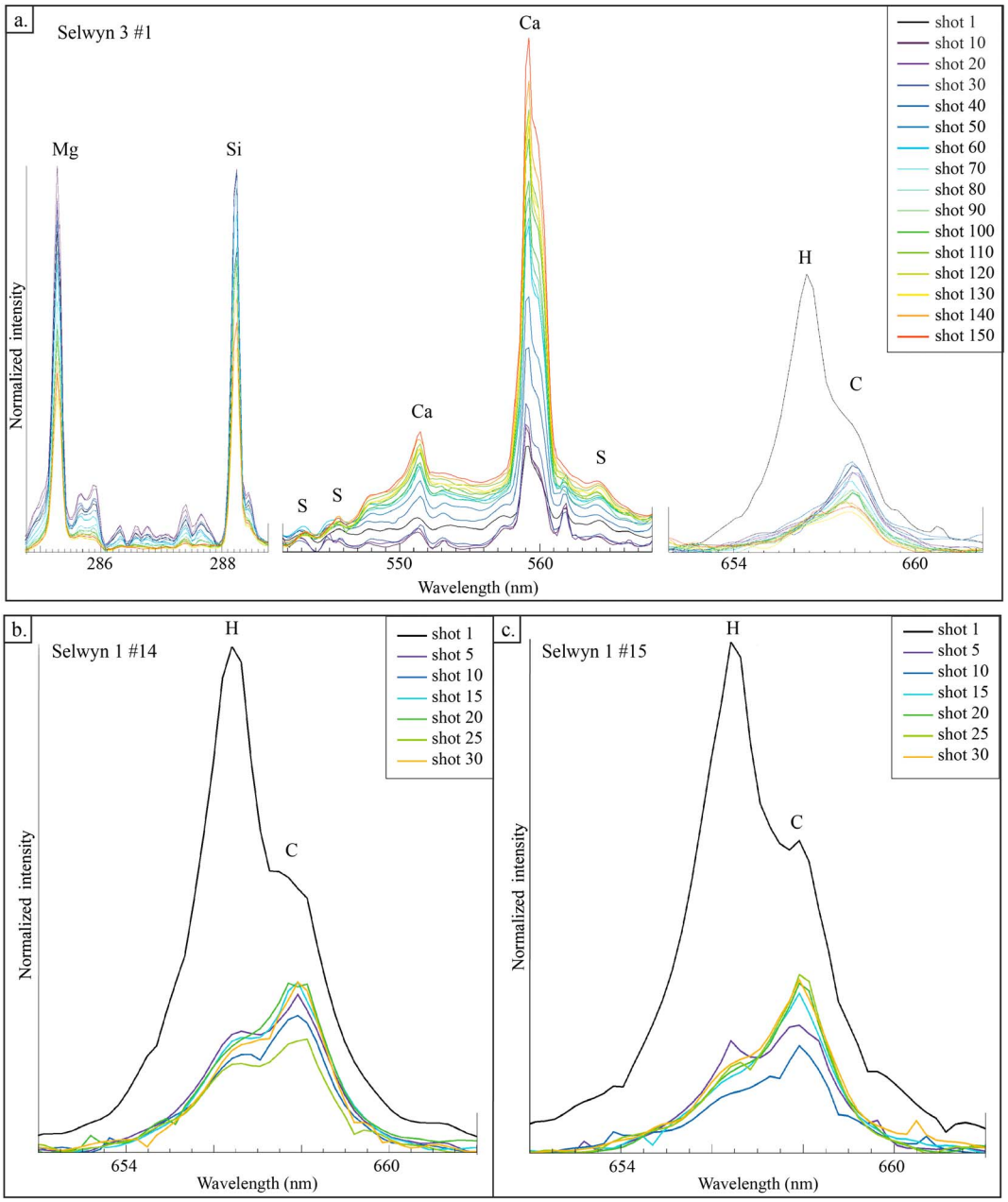

Figure 6. Variations along depth profiles, at various points of the target Selwyn. (a) Depth profile of 150 shots made at point 1 (#1) of the target Selwyn 3. The inverse trend of Ca and S compared with Si and Mg shows an enrichment of calcium sulfates at depth. Hydrogen is very low, except from the first shots, that correspond to the dust [see *Meslin et al.*, 2013]. Spectra shown along 30 shots made at (b) points 14 and (c) 15 of the target Selwyn 1. Location 14 does show stable H all through the depth profile. Location 15 appears less clear in terms of an H signature at depth, suggesting either nonhydrated or poorly hydrated calcium sulfates. For Figures 6a–6c, the intensity of the lines is relative to each portion of the spectra.

effects could be stronger than the difference in the emission line of H related to its proportion inside the mineral. Thus, the approach taken here and reported on Table 1 is to identify H from the presence of the emission line, without trying to enter into a more detailed phase identification.

Point 6 of the Fury target and point 5 of Mavor show the presence of H lines (Figure 5), as do many other calcium sulfate targets. This suggests that the calcium sulfates observed include hydrated sulfates such as gypsum and bassanite. By comparison, the calibration target is dry and does not show any H lines, as do Mavor and Fury analysis (Figure 5a). A noticeable exception is appreciable for the outcrop Selwyn, analyzed 4

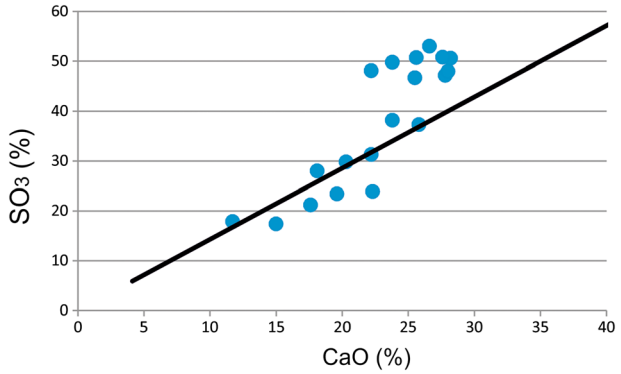

Figure 7. Plot of CaO versus SO_3 using results from the PLS on selected targets for which sulfur was detected. The straight line indicates the stoichiometry of calcium sulfates ($CaSO_4$).

times by ChemCam (targets Selwyn, Selwyn 1, Selwyn 2, and Selwyn 3). It displays various points with calcium sulfate signature, including several with either no or only very weak H emission, suggesting the presence of anhydrite (Figures 6a and 6c).

Depth profiles may aid in determining whether hydration is linked to the mineral itself or to thin surface layers that could have been hydrated from contact with the atmosphere. The target Selwyn 3 consisted of four laser locations of 150 shots each, for deeper analyses (whereas, for example, on Figure 5c, the orange spectrum is the average of 30 shots at point 8 of the target Selwyn). An increase of Ca associated with a depletion in all other major elements, coupled to the observations of sulfur peaks, shows that this point analysis contains calcium sulfate. Figure 6a shows that the composition changed from the first shots to the last ones over the 150 shots. Initially, H is high, corresponding to dust, but the other spectra do not contain H, or only a very small peak can be seen for shot 150 (orange). These data therefore are consistent with a relatively pure calcium sulfate overlain by a thin layer of dust.

Locations using the nominal 30 laser shots represent smaller depth profiles that may still be able to show trends in the hydration phases. Location 14 of Selwyn 1 (Figure 6b) shows an H signature that is stable over the 30 shots. In contrast, location 15 of Selwyn 1 (Figure 6c) has an H monotonically decreasing after shot 5. In this case, it is difficult to determine if the H signature is associated with the inferred Ca sulfate material. In Table 1, we consider the Ca sulfate mineral of Selwyn 3 location 1 (Figure 6a) to be nonhydrated, that of Selwyn 1 location 14 (Figure 6b) to be hydrated, and that of Selwyn 1 location 15 (Figure 6c) as possibly hydrated and requiring more detailed analysis.

3.3. Quantification of the Elemental Composition

Multivariate analysis techniques such as partial least squares (PLS) have been developed to extract elemental compositions from LIBS spectra [*Clegg et al.*, 2009; *Wiens et al.*, 2013]. For ChemCam elemental analysis, customized PLS1 models were created for each of eight major elements including SiO_2, TiO_2, Al_2O_3, FeOT, CaO, MgO, Na_2O, and K_2O. Unfortunately, simple PLS analysis of the preprocessed spectra does not result in quantitatively reliable models for elements such as sulfur that produce small emission lines compared to the major elements. All other minor elements tend to produce weak emission lines simply due to their low abundance in the sample. For these elements, we have employed a new method of integrating all of the emission from each individual emission line and assigning that intensity into the single pixel with the highest intensity [*Clegg et al.*, 2009]. Consequently, the LIBS spectra have been reduced from 6144 individual pixels to typically 500 pixels, and the weaker emission lines have enough intensity to be relevant to the PLS1 analysis. This method was used to extract the SO_3 oxide weight percents (Figure 7 and Table 2).

This method does not allow one to distinguish hydrated minerals from the ones that are not hydrated because H is difficult to quantify and is not included into the PLS code. Thus, comparison of this quantification is only relevant for nonhydrated calcium sulfate (anhydrite, $CaSO_4$), for which the stoichiometry is CaO = 41.2% and SO_3 = 58.8%. Contamination by surrounding rock or soil is still present in many points as shown from the presence of 10 to 30% SiO_2 and a few weight percent of other elements (Table 2). Plotting CaO versus SO_3 allows us to observe the related increase of calcium and sulfur (Figure 7), mainly along a straight line that matches the stoichiometry of calcium sulfate. The highest SO_3 content seems to deviate from this trend. The deviation could be due to an idiosyncrasy in the PLS model, given that it is at relatively high calcium abundance, well away in compositional space from the majority of the training set, although it does contain five gypsum standards [*Wiens et al.*, 2013]. Another possible factor could be an

Table 2. Quantitative Composition (in Weight Oxide %) From PLS of Selected Targets With Calcium Sulfates Identified

	Point of Target	SiO_2	Al_2O_3	FeOT	MgO	**CaO**[a]	Na_2O	K_2O	**SO_3T**[a]	Sr (ppm)	Total
RMSEP		7.1	3.7	4.0	3.0	**3.3**	0.7	0.9	<5	430	10.1
Rapitan	1	21.8	4.6	8.3	7.0	**22.3**	0.7	0.0	**23.9**	320	89.7
	2	10.6	1.9	1.9	7.7	**26.6**	0.0	0.0	**53.0**	400	102.8
	4	12.1	1.9	2.9	9.2	**27.8**	0.0	0.0	**47.2**	450	101.9
	5	10.8	2.4	2.4	5.9	**28.0**	0.4	0.0	**48.0**	370	98.9
	6	12.2	1.7	1.7	8.4	**28.2**	0.0	0.0	**50.6**	380	103.6
	7	32.2	6.0	12.0	6.5	**15.0**	1.9	0.0	**17.4**	310	92.1
	8	10.6	2.3	0.7	5.0	**25.5**	0.5	0.0	**46.7**	390	91.9
	9	11.5	2.3	2.3	8.1	**27.6**	0.0	0.0	**50.8**	400	103.8
Selwyn	8	16.9	3.7	5.9	2.9	**22.2**	1.3	0.0	**31.3**	320	84.8
Selwyn 1	14	25.7	5.1	11.3	2.0	**17.6**	1.5	0.0	**21.2**	340	85.4
	15	32.6	4.8	13.5	7.3	**11.7**	1.5	0.0	**17.9**	340	90.5
Selwyn 2	3	16.2	2.7	4.1	1.6	**25.8**	0.8	0.0	**37.3**	360	89.2
	5	29.5	6.5	12.1	5.1	**19.6**	1.4	0.0	**23.4**	280	98.8
Mavor	5	14.1	2.3	2.3	6.7	**22.2**	0.1	0.0	**48.1**	400	96.7
	6	12.0	1.0	1.0	6.4	**23.8**	0.0	0.0	**49.8**	360	94.7
Thundercloud	2	28.9	4.7	9.5	6.6	**20.3**	1.7	0.0	**29.8**	330	101.6
Seward 1	4	24.1	5.3	8.8	4.0	**18.1**	1.5	0.0	**28.0**	320	90.8
	5	11.8	1.5	1.9	7.3	**25.6**	0.0	0.0	**50.7**	340	99.7
Fury	6	12.2	3.4	2.5	2.8	**23.8**	1.3	0.0	**38.2**	370	84.8

[a]Main chemical elements (Ca and S) present in calcium sulfates are presented in bold.

underestimation of the CaO when lines are very high due to self-absorption of intense emission lines; i.e., emission can be suppressed in the plasma if present in too large abundance. A detailed statistical approach would be limited by the ~5% of Root Mean Square of Error Prediction (RMSEP) that generates large approximations. In general, the relatively good correspondence of CaO and SO_3 to the expected calcium sulfate stoichiometry as shown in Figure 7 confirms the overall conclusions obtained from the individual spectra that the identified minerals are indeed calcium sulfates. It demonstrates that no other element but sulfur is required in significant proportion.

3.4. Minor and Trace Elements

ChemCam can also identify several minor and trace elements, which can be useful in tracing origins of precipitating fluids. As presented in Figure 8a, Sr is higher in calcium sulfates points (full lines) relative to the surrounding ChemCam analysis. This is expected because Sr readily substitutes for Ca in a variety of minerals, despite the preference for Sr to remain in the fluid phase [e.g., *Turekian and Kulp*, 1956]. Within the Selwyn 3 depth profile at point 1, Sr shows the same trend as Ca, demonstrating its presence in relation to the sulfate phase (Figure 6a).

Estimates of Sr abundances are obtained from the partial least square (PLS) models presented in *Ollila et al.* [2013]. A generalized model for all geologic matrices including calcium sulfates gives an average Sr abundance of 360 ± 430 ppm Sr for the high-Ca locations listed in Table 2. By comparison, the average Sr abundance in the host rock for these same targets is 40 ± 160 ppm, which was calculated using an igneous-like matrix model over points that have positive abundance estimates. To further constrain Sr abundances in calcium sulfates, a matrix-matched model containing only calcium sulfates is required.

Other trace elements, Rb, Ba, and Li, were found in rocks along the rover traverse [*Ollila et al.*, 2013]. Those are not detected in significant abundances in the calcium sulfates. Figures 8a and 8b show sections of spectra with barium peaks as identified in one ChemCam calibration target (dotted black line), but this element does not show peak at these spectral wavelengths in the calcium sulfates analyzed (full lines). Other minor elements have been searched for, such as Zn, but have not been identified.

3.5. Passive Spectra Analyses

Most passive spectra collected during the first year of operations exhibited a ferric absorption edge in the visible region (<600 nm) and maximum reflectance values near 0.25, typical of dusty Martian soils [*Johnson et al.*, 2014]. However, LIBS observations indicating sulfur and high Ca consistently exhibited corresponding

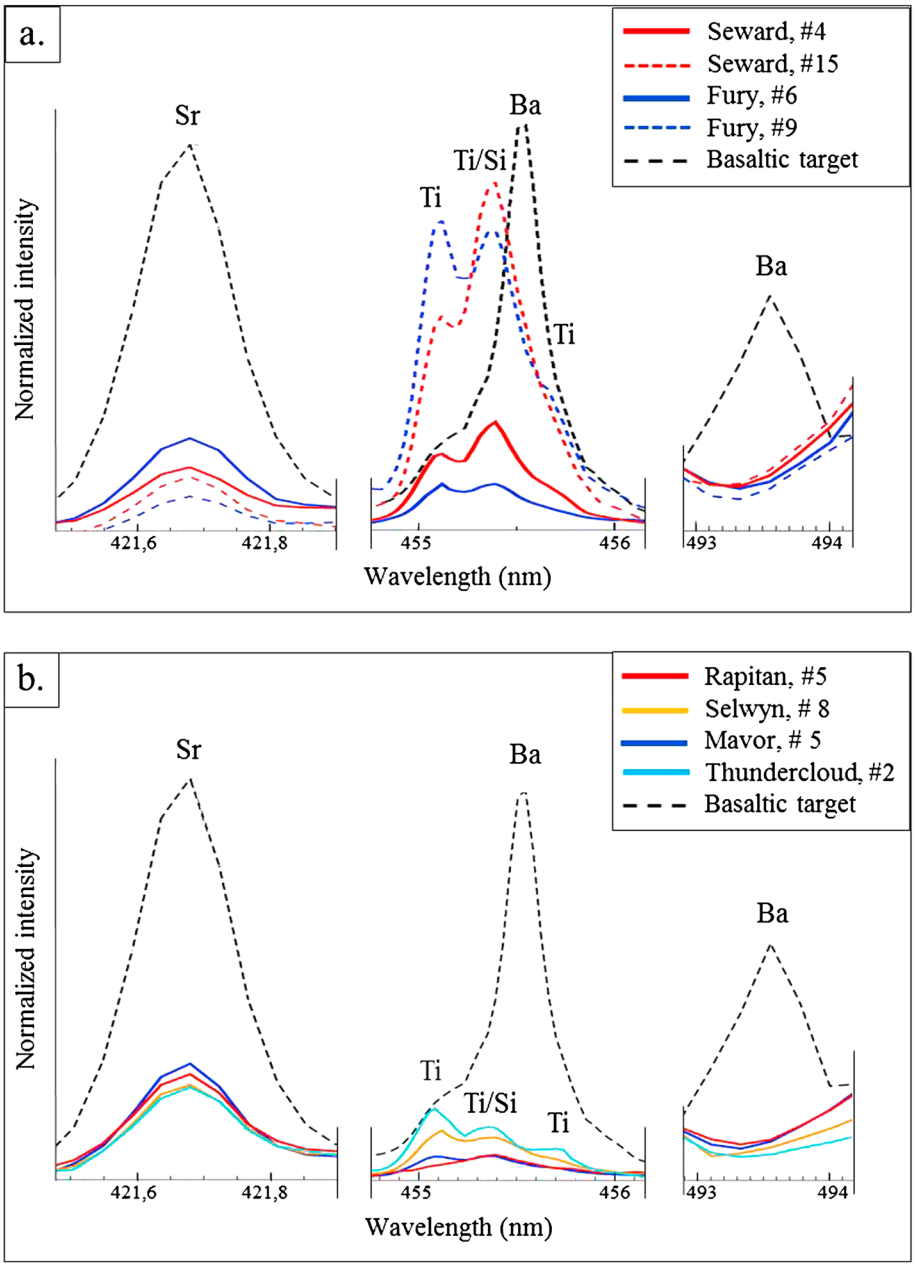

Figure 8. (a and b) Minor elements potentially detectable in ChemCam calcium sulfates: Sr at 421.67 nm; Ba at 455.53 and 493.5 nm [see *Ollila et al.*, 2013]. For calcium sulfate points (full lines), Sr is higher than for surrounding points (dotted blue and red lines). The ChemCam calibration basaltic target (dotted black line) has 200 ppm by comparison (this target was especially enriched in Sr) The identification of barium is at the detection limit.

passive spectra with the highest relative reflectance values (above 0.50) of all targets observed. Figure 9 shows such spectra from Rapitan (sol 135) and Measles Point (sol 306), along with a typical relative reflectance spectrum from the surrounding rock in the mudstone member at Rackla (sol 135). Spectra on calcium sulfate minerals have higher reflectance values and less spectral reddening than the ChemCam passive spectra on surrounding rocks.

Also shown on Figure 9 are laboratory spectra for the calcium sulfate minerals gypsum, bassanite, and anhydrite. Within the lab spectra used, the comparison of ChemCam passive spectra with those spectra suggests that anhydrite is a poor candidate, whereas both gypsum and bassanite are plausible candidates. Nevertheless, the lack of distinctive features at these wavelengths does not allow bassanite to be distinguished from gypsum as

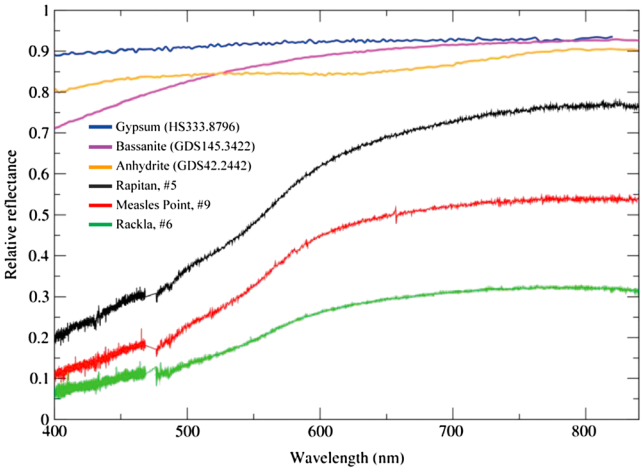

Figure 9. ChemCam relative reflectance spectra (400–840 nm) of the identified Ca sulfate at Rapitan (sol 135, point 5) and at Measles Point (sol 305, point 9) compared to typical Sheepbed bedrock spectra from Rackla (sol 135, point 6) and laboratory spectra of calcium sulfate minerals from *Clark et al*. [2007] convolved to ChemCam wavelengths.

can be done using Mastcam's longest wavelength filters [*Rice et al*., 2013; *Bell et al*., 2013]. The best candidate for anhydrite based on the lack of an H peak in the LIBS spectrum was a sample near Selwyn which was in the shadow during the observation and therefore it does not have a useable passive spectrum.

4. Geological Settings of Calcium Sulfates Inferred From ChemCam Data

4.1. Observations of Texture on RMI Images and Cross-Comparisons With Elemental Composition

RMI images of all targets were performed before and after firing the laser, enabling us to identify the locations of the laser shots. Every Ca sulfate detection corresponds to light-toned material distinct from surrounding rocks (Figures 10, 11, 14, and 16). We first provide the details of the targets located within the Sheepbed mudstones, where they are by far more numerous and then extend the observations to other outcrops in the next section. Their texture can be divided into three distinct categories, described below.

Elongated light-toned fracture fills compose a large fraction of all observations, including Seward 1 and Fury targets, the spectra of which are presented in Figures 3–5. These veins are usually thin (<2 cm wide) and crosscut the rocks in different a variety of orientations, following subvertical to nearly horizontal planes (Figures 10a–10d). In terrestrial occurrences, gypsum crystals can grow orthogonal to fracture planes, generating parallel crystal fibers, referred to as fibrous or "palisade" gypsum (see Figure 12 for a terrestrial analogue) [e.g., *Richardson*, 1920; *Warren*, 1999]. None of the RMI images of veins, however, has shown any texture, or relics of typical fibrous gypsum. The LIBS spectra of light-toned veins all display positive detections of Ca sulfates, with largely prevalent hydrated forms (Table 1).

Second, individual nodules or series of nodules are observed in outcrops such as Ruth, Cumberland, and Mavor (Figures 10e–10g). The largest nodules reach 2 cm across and display irregular contours. Smaller nodules include so-called bowls, which are subspherical and several millimeters in diameter. In many cases, nodules align along fractures and thus produce a somewhat transitional texture between veins and isolated nodules (Figure 10c, top), suggesting a genetic link between both types of features. All LIBS spectra obtained from light-toned nodules and bowls have positive detection of Ca sulfates, and most show evidence for hydration (Table 1).

Third, several outcrops display light-toned material with polygonal texture at the millimeter to centimeter scale. At Rapitan (Figure 10h), erosion has apparently exposed a light-toned feature with very clear Ca sulfate signatures (Figures 3 and 4). At Richardson 2 (Figure 10i), the light-toned material protrudes at the surface as a vertical blade, likely corresponding to the relic of a former sulfate vein more resistant to erosion than the embedding mudstones. At Selwyn outcrop, a remarkable light-toned nodular texture is exposed and is part of a complex assemblage of light-toned veins (Figure 11). The surface is steep, suggesting that the nodular texture does not fill the nearly vertical fractures as elsewhere (Figure 11). Actually, this nodular texture comprises the bounding unit of two distinct lithologies. The upper one displays a rough surface with cemented, sand-sized grains typical of the Gillespie member, whereas the lower unit is softer and homogeneous, except for local hollow nodules that are common within the Sheepbed mudstone. The nodular texture thus bounds the Sheepbed member below it from the Gillespie sandstones on top. Hydration is varied on these Selwyn targets (Table 1). Four out of the six points with Ca sulfates do not present hydrogen signature, or a very low emission, suggesting the presence of anhydrite.

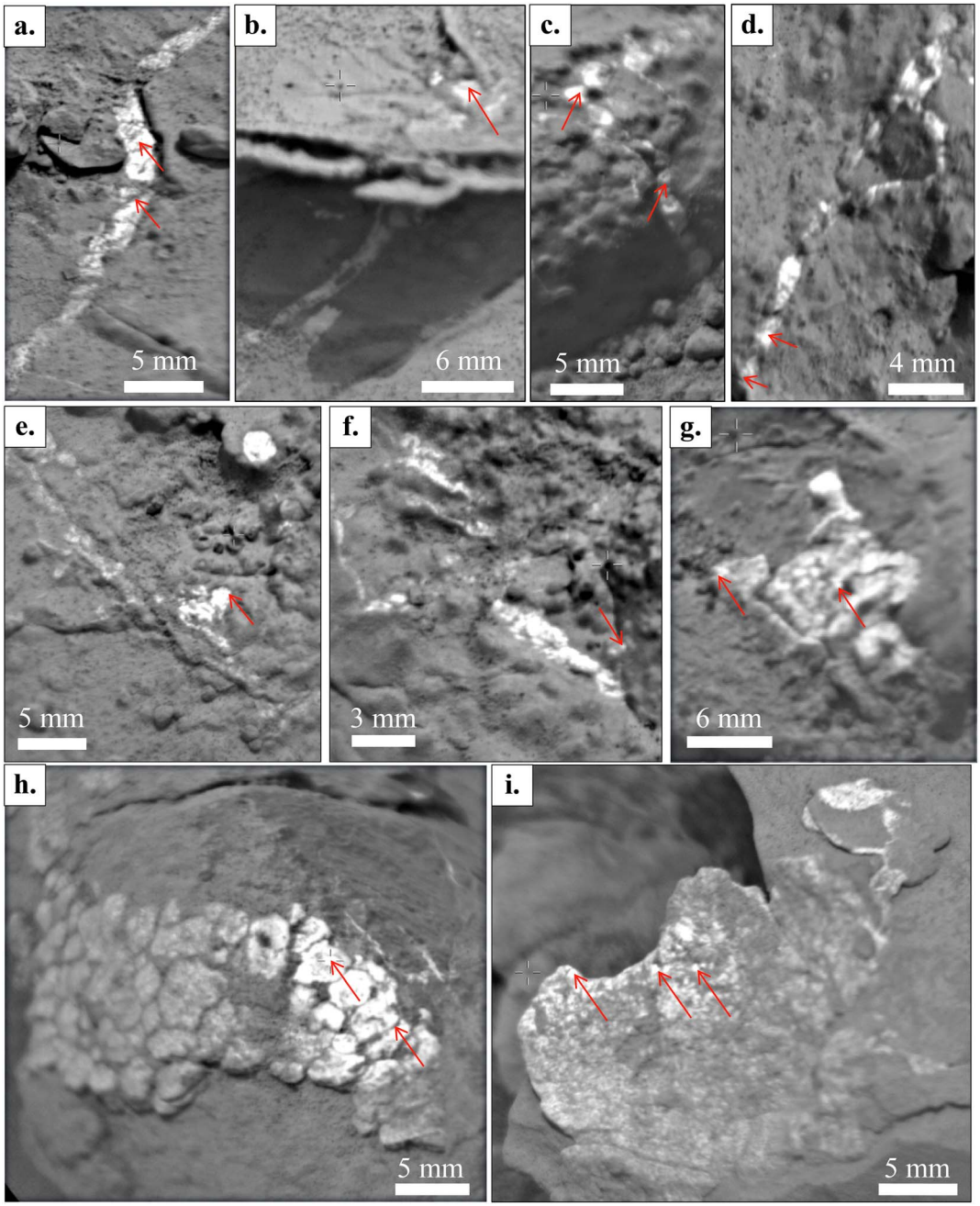

Figure 10. Textures of ChemCam calcium sulfates targets inside the Sheepbed unit as seen by ChemCam/RMI: (a) Tukarak (sol 165); (b) John Klein RP3 (sol 165); (c) Ruth (sol 232); (d) Seward 1 (sol 187); (e) Cumberland Bowl (sol 275); (f) Cumberland 3 ccam (sol 292); (g) Mavor (sol 160); (h) Rapitan (sol 135); (i) Richardson 2 (sol 130). Locations shot by ChemCam with positive identification of calcium sulfate are shown with red arrows.

Light-toned features at Rapitan (Figure 10h) are close to that of Selwyn, with a polygonal texture separated by darker material. LIBS analyses at Rapitan reveal nevertheless the presence of hydrogen, at a low level, suggesting that the Ca sulfate material may correspond to the intermediary phase bassanite. At Richardson 2, small sub-millimeter-wide polygons can be observed at the surface of this blade, for instance, immediately right of the most right red arrow pointing toward the ablated spot. These are distinct from the larger nodular texture and suggest that dehydration may have taken place. A similar texture is observed in individual nodules such as Mavor (Figure 10g).

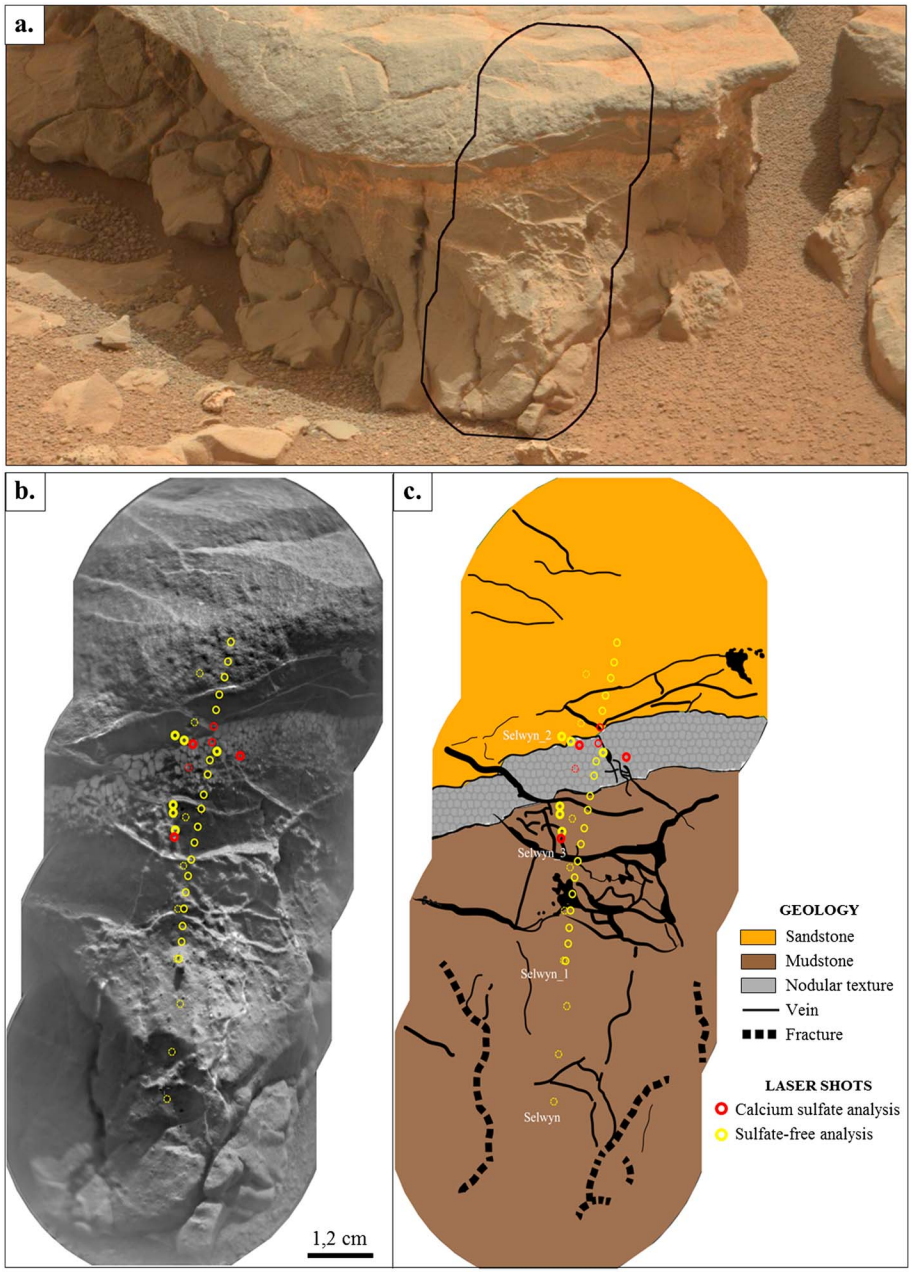

Figure 11. Detailed investigation of Selwyn targets (sols 154 to 159): (a) Mastcam image of Selwyn outcrop. The black figure shows the (b) ChemCam/RMI close-up. The dots represent the laser shots from the 1 × 10 raster Selwyn, the 1 × 20 raster Selwyn 1 (both starting from bottom), the 5 × 1 raster Selwyn 2 (starting from left), and the 2 × 2 raster Selwyn 3. Points shot by ChemCam with positive identification of calcium sulfate are shown with red dots; yellow dots represent sulfur-free analyses. (c) Geological sketch with veins (black lines) and the nodular texture (gray) which separates the underlying mudstone Sheepbed (in brown) from the overlying sandstones Gillespie (in orange).

A more detailed look at the nodular textures is possible. The Selwyn nodular texture is composed of vertically elongated, variably coalescent displacive nodules. In terrestrial sedimentary strata, such nodular textures, sometimes referred to as "chicken-wire" texture (Figure 12b), are generated by the primary displacive growth of sulfates that pushed around original insoluble impurities of the sediment, which later form a film around nodules [*Kerr and Thompson*, 1963; *Warren*, 1982; *Shearman*, 1985; *Hussain and Warren*, 1989]. The displacive gypsum either is precipitated from hypersaline Ca-sulfate-saturated interstitial fluid that increases in salinity as it rises by capillarity action from the water table to the surface, i.e., early diagenesis in which proper

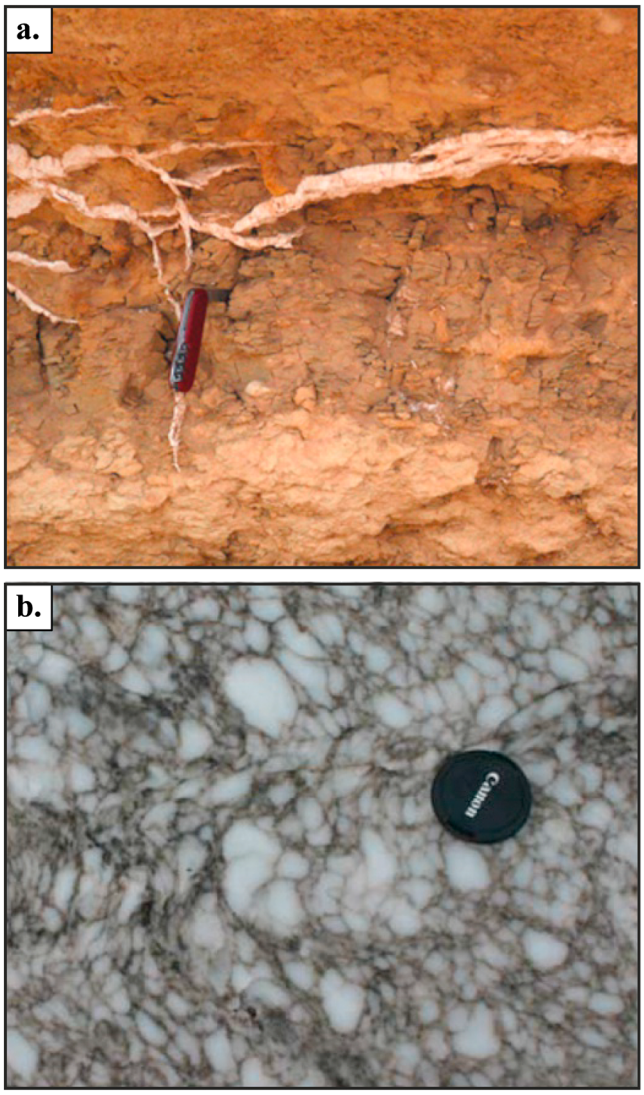

Figure 12. Terrestrial analogues to some of the features observed. (a) Gypsum veins in Egypt in a sabhkha environment (NASA/JPL-Caltech/LANL/CNES/IRAP/IAS/LPGN/CNRS/LGLyon/Planet-Terre/P. Thomas). (b) Example of nodular texture ("chicken wire") from sulfate fills in Svalbard [*Nanfito*, 2008]. Credit: A. F. Nanfito.

chicken-wire textures are developed, or is the result of dehydration/rehydration of subaqueous gypsum during burial/exhumation of sediments, i.e., late diagenesis. At Rapitan, nodules are grouped into composite nodules that produce incipient contorted folds that may be enterolithic [e.g., *Warren*, 1999; *Schreiber and El Tabakh*, 2000], a texture also typical of anhydrite, but at the resolution of the image this interpretation remains speculative.

The material between the nodules has the typical chemical signature of the Sheepbed mudstone, as confirmed from the LIBS spectra from two locations, supporting the interpretation that the nodules grew displacively. It should also be emphasized that none of more than 500 locations that were shot within the Sheepbed mudstone surrounding the light-toned veins and nodules display evidence of sulfur (within detection limit) and high-calcium phases. The indication of limited lateral continuity of the nodular texture is more consistent with some early nodule growth close to the surface rather than any extensive replacement of original subaqueous gypsum beds. The fact that the nodular layer lies immediately beneath the Gillespie sandstone bed might reflect the development of a permeability barrier. The 2 cm thick nodular texture of probable anhydrite is crosscut by thinner veins which become more horizontal as they enter into the overlying unit, showing that differences in mechanical properties are important and could have induced a flattening of fractures in less brittle levels. Some early cementation of the sandstones could have restricted the rise of the water table and favored its saturation at this location.

4.2. Observations of Texture From Other Imaging Instruments

In addition to ChemCam observations of texture and composition, Mastcam and MAHLI images provide more details on their setting.

At the scale of the outcrop, veins infilling occur primarily within broadly planar fractures. Sulfate-filled fractures are visible in a variety of lengths, from less than 1 cm to greater than 60 cm, and are observed to penetrate up to tens of centimeter of vertical section (Figure 2). These fractures are diverse in their orientation, from near vertical to subhorizontal, and short fracture lengths likely represent visible portions of a more complex fracture network. Where visible, changes in fracture orientation occur abruptly: within potentially homogeneous mudstone regions, at the interface of

mineralized raised ridges [*Grotzinger et al*., 2013; *Siebach et al*., 2013], and between adjacent hollow nodules [*Grotzinger et al*., 2013; *Stack et al*., 2013] (Figure 15). Where calcium sulfate veins intersect hollow nodules, mineralization commonly infills voids, forming spheroidal blebs.

Another textural element that can be useful in terms of constraining environments of deposition is the internal crystal structure within veins, with local fibrous gypsum, which can be classified as either antitaxial or syntaxial [*Durney and Ramsay*, 1973; *Dong et al*., 1995; *Bons*, 2000]. Antitaxial veins are represented by a single surface of crystal nucleation in the center of a closed fracture, followed by crystal growth outward, toward the fracture walls. In cases where there is no lateral shear, antitaxial growth results in fibrous crystal growth perpendicular to the fracture walls, and crystal growth is the primary mechanism for dilation of the fractures in an environment otherwise characterized by sufficient overburden as to not permit open fractures. By contrast, syntaxial growth occurs within more shallowly emplaced, open fractures. In this case, crystal nucleation occurs on fracture walls, and growth occurs inward, toward the center of an open crack. Crystal orientation in syntaxial vein fills is typically much more variable and often indeterminant. Internal vein textures are not clearly apparent within either veins or nodules, as observed by Mastcam, MAHLI, and RMI, thus limiting interpretations. Nevertheless, the lack of obvious fibers at that scale is consistent with potentially shallow ($<$3 km) emplacement of fractures and vein fills.

Such characteristics are reminiscent of fracture networks generated by hydraulic fracturing [*Shearman et al*., 1972; *Gustavson et al*., 1994; *Cosgrove*, 2001; *Philipp*, 2008]. Hydraulic fracturing occurs when pressurized liquid creates tensional fractures through overlying rock, due to hydrostatic pressures exceeding lithostatic pressures and the yield strength of the rock. Commonly, these same fluids, which can result from dehydration during burial compaction or mineral dehydration such as smectite or gypsum phases, are the source of mineralization, as well [*Osborne and Swarbrick*, 1997]. The relatively low permeability of mudstone units permits buildup of hydraulic pressure until the strength of the lithified mudstone is overcome and fracturing ensues. In the case of Sheepbed fractures, veins are predominantly vertically oriented, suggesting sufficient hydraulic pressures to facilitate fracture propagation in the direction of the greatest compressive strength. However, the observation that veins reorient themselves, for example, along margins of raised ridges, suggests that hydraulic pressures were not sufficient to penetrate more heavily mineralized regions. Other veins that occur parallel to bedding, or that meander through concentrations of hollow nodules, suggest that at least some of the hydraulic pressure exploited inherent zones of weakness within the Sheepbed mudstone.

Combined with the RMI observations, these observations suggest that fractures and calcium sulfate mineral infill occur as a late-diagenetic phase, postdating early diagenetic formation of raised ridges and nodules that are characteristic of the Sheepbed member [*Grotzinger et al*., 2013]. Sharp contacts between mineral infilling and host rock, as well as abrupt change in fracture direction, indicates that sedimentary strata were well lithified prior to formation of fractures. Crosscutting relationships, where visible, do not show any clear distinction between mineral infilling in different veins, suggesting that all the veins may have formed as part of a single diagenetic event that affected both fracture formation and mineral infill. An exception may come from observations at Selwyn. As thin veins crosscut straight across the nodular texture, a multiphase emplacement is likely there. However, primary anhydrite (formed by lacustrine evaporation and fluid precipitation at the surface with enhanced evaporation) is not necessary. Observations better suggest general late-stage diagenetic processes, with perhaps a relatively earlier diagenetic setting for the nodular anhydrite compared to thinner veins.

4.3. Geological Distribution

The location of all targets identified as calcium sulfates enables a mapping of their distribution throughout the YB area (Figure 13). A large majority of targets with calcium sulfates are found inside the Sheepbed member (e.g., Seward 1, Rapitan, and Mavor). This is interpreted as a direct consequence of the weak strength of clay-rich mudstones allowing cracks to form more easily than in well cemented sandstones. However, this predominance may be biased due to the extended time spent by the rover inside this unit (from sols 125 to 295), which was selected for the two drill holes, whereas the characterization of the other outcrops was not as extensive.

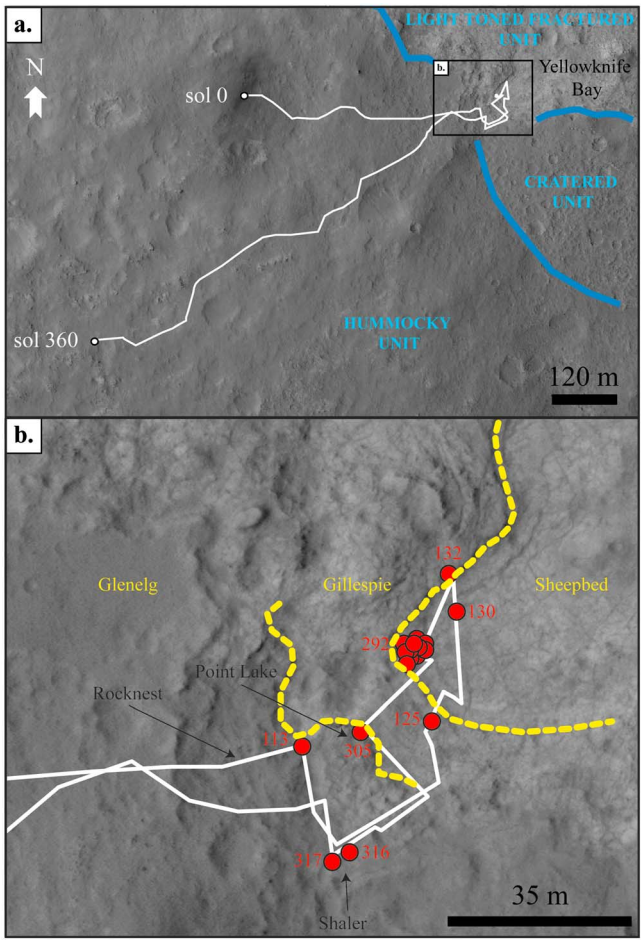

Figure 13. Geographic distribution of the ChemCam calcium sulfate targets (red dots) along the Curiosity rover route (white line) up to sol 360. From HiRISE image ESP_028335_1755. Numbers in red indicate the sol. Only the series of sediments identified at Yellowknife Bay display calcium sulfates.

Notable detections of calcium sulfate, however, also occur within other members of the Yellowknife Bay formation. Overlying the Sheepbed member are thin, coarse-grained resistant sandstone beds of the Gillespie member. In general, vein-filled fractures at Gillespie are heterogeneous in density, with some locations poorly fractured and other locations containing relatively dense fracture networks. The outcrop where the target Crest was chosen is stronger than the mudstones, as shown from the scarp at the edge of the outcrop (Figure 14a), but it is strongly fractured, with thin veins visible in the RMI image. Two analysis points were attributed to calcium sulfates there. The outcrop at Selwyn (Figure 11) shows that veins cut through the contact between Sheepbed and Gillespie. This implies a formation of these veins subsequent to the deposition of the uppermost layers.

The overlying Glenelg member also contains several calcium sulfate detections, although discrete veins are uncommon within these generally coarser-grained units. Resistant, coarse-grained, vuggy rocks of the Point Lake outcrop display two detections: Bell Island 1 and Measles Point (Figures 14b and 14c). At Measles Point, the 0.5 m high outcrop encountered on the way out of YB shows abundant fractures, with partial filling by light-toned material. The ChemCam detection of calcium sulfates corresponds here to a 5 mm large nodule preserved from erosion at the surface of the rock (Figure 14c). The observation at Bell Island 1 shows several very thin light-toned veins (bright centimeter-sized lineations on the Mastcam image) crossing the rough rock surface. These veins are much smaller and less developed than in the Sheepbed unit. The Bell Island 1 vein shown in the RMI image was analyzed at the first location of the 3 by 3 matrix, and it corresponds to the first confirmed calcium sulfate detection, on sol 113, before entering into the Sheepbed area.

Finally, two detections of calcium sulfate were confirmed within the Glenelg member Shaler outcrop. The Shaler outcrop sits, at places, above the Point Lake outcrop and is composed of interbedded siltstone and sandstones with abundant cross-stratification [*Grotzinger et al.*, 2013; *Edgar et al.*, 2013]. Relatively wide veins cross this outcrop, but in much lesser number than in the Gillespie and Sheepbed members (Figures 1 and 15). Two ChemCam targets, Reddick Bight (Figure 14d) and Denault (Figure 14e), contain calcium sulfates both corresponding to thin veins. Some of these veins partly follow laminations, suggesting a preferential filling of the voids or softer material between laminae. Other veins cross the layers more orthogonally.

The Rocknest material, located at the highest point topographically of these sediments, possibly represent a degraded outcrop but has an unclear stratigraphic contacts with respect to other faciès observed in the Glenelg member [*Grotzinger et al.*, 2013]; it does not display any clear evidence for

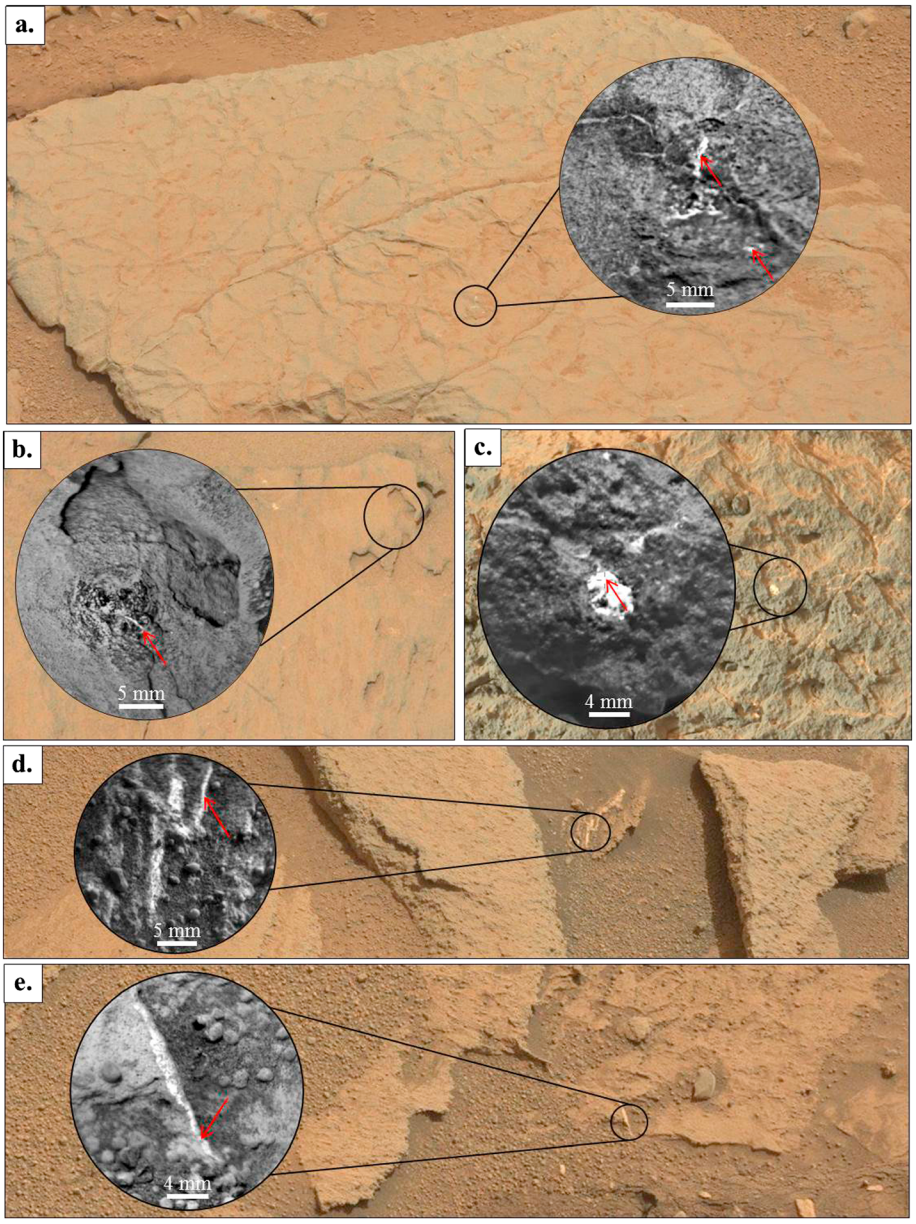

Figure 14. Examples of ChemCam calcium sulfate targets as seen by the ChemCam/RMI (black and white close-ups), within different units as seen in color by Mastcam. (a) Crest within Gillespie; (b) Bell Island 1 and (c) Measles Point, within Point Lake; (d) Reddick Bight and (e) Denault within Shaler outcrop. Red arrows are ChemCam points with positive identification of calcium sulfate.

calcium sulfate veins. A few high-calcium phases were nevertheless detected, but these are proposed to include phosphates [*Forni et al.*, 2014]. Cracks are present inside the Rocknest material, but no light-toned material fills those fractures.

Thus, calcium sulfate veins are found along most of the 4–5 m thick stratigraphy of Yellowknife Bay showing that at least some of the veins are late-stage diagenetic features formed well after all these sediments were deposited, with the possible exception of rocks from the Rocknest area. All calcium sulfates found during sols 0 to 360 are seen to crosscut the YB formation strata, and all veins analyzed between sols 113 and 317 are consistent with a Ca-sulfate composition. The Sheepbed mudstone surrounding the light-toned veins and nodules display no evidence of sulfur (within limitation of the small spectral feature) and high-calcium phases, suggesting a rather distinct chemistry.

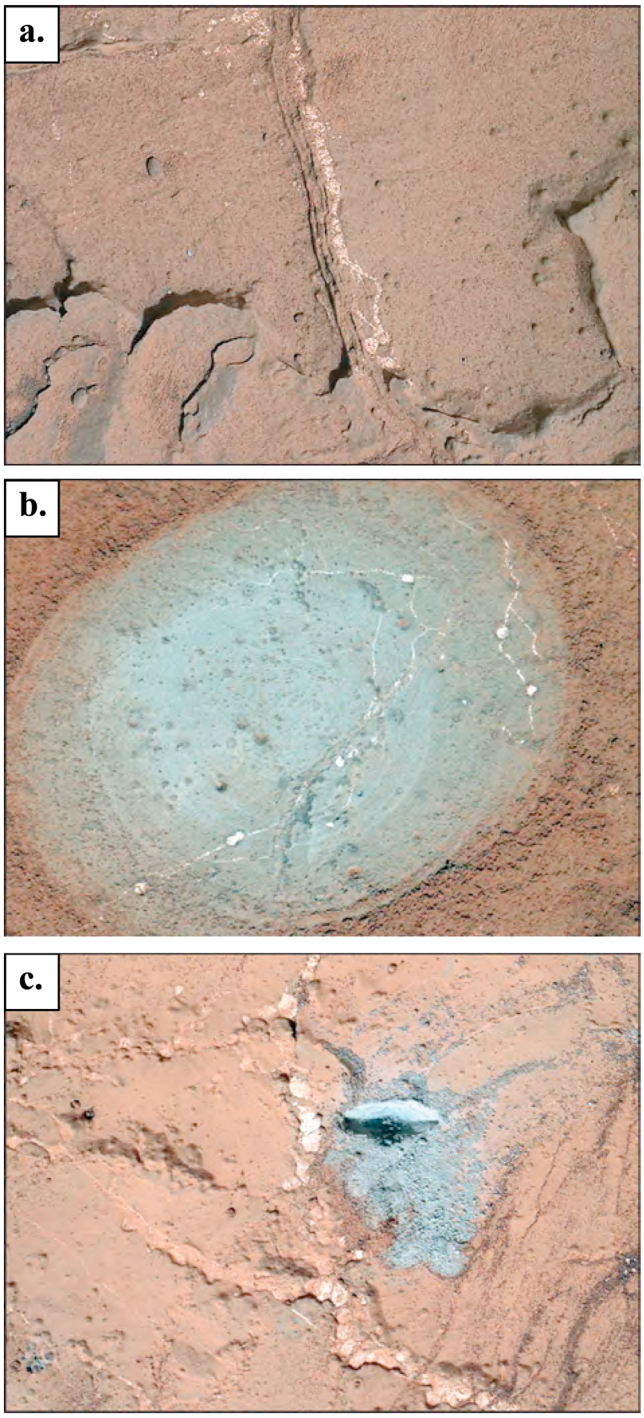

Figure 15. MAHLI images revealing structure of light-toned veins. (a) Three millimeter thick vein aligned next with early diagenetic raised ridges, suggesting that fracture formation was unable to penetrate heavily lithified areas. (b) Multiple-orientation, hairline fractures penetrating discrete 3–5 mm diameter nodules. (c) Six millimeter wide irregular vein that suggests formation in part via filling of closely spaced hollow nodules.

5. Discussion

5.1. Observations of Sulfates in Veins by Other Instruments

In addition to ChemCam, Curiosity's CheMin, Mastcam, and Alpha Particle X-ray Spectrometer (APXS) instruments were used to investigate YB. The first drilled samples were collected on John Klein and Cumberland (in the Sheepbed mudstones). CheMin X-ray diffraction analysis indicated the presence of both anhydrite and bassanite, but not gypsum [*Vaniman et al.*, 2013]. One drill hole was targeted by ChemCam along 10 points from bottom to top (Figure 16). The seventh point hit a thin, light-toned vein, visible in the RMI image, which contains elevated Ca and S, consistent with other veins analyzed nearby (Table 1). The very low hydrogen intensity observed in the ChemCam spectra points toward the presence of anhydrite in this vein, in agreement with the CheMin analysis. This example suggests that not only nodular texture but also narrow veins can contain anhydrite.

Similarly, the APXS instrument investigated Mavor, one of the largest nodules observed, and determined that its composition was indeed consistent with $CaSO_4$ [*McLennan et al.*, 2013]. As APXS is not able to detect hydrogen, no determination of the hydration state was possible.

Lastly, Mastcam multispectral images were used to infer the presence of gypsum. Indeed, gypsum displays a very specific narrow absorption band at 1.03 μm [*Bell et al.*, 2013]. Whereas gypsum can be strongly inferred from Mastcam spectral analyses, bassanite does not present the same signature, allowing Mastcam to provide some discrimination between the two hydrated phases. The Mastcam observations conducted during the YB campaign are consistent with the presence of gypsum in multiple locations [*Vaniman et al.*, 2013; *Rice et al.*, 2013]. However, numerous other veins do not display similar spectral feature, suggesting that other phases are present, namely, bassanite and/or anhydrite as described by ChemCam observations.

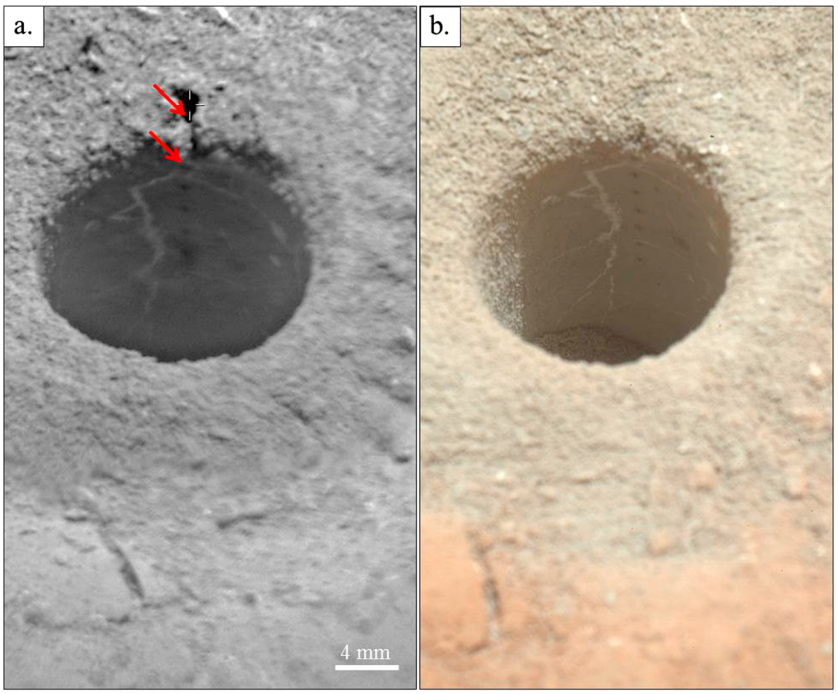

Figure 16. Texture and localization of ChemCam calcium sulfate on points 7 and 9 (red arrows) within the drill hole, as seen (a) by the ChemCam/RMI and (b) by MAHLI 43 sols later.

5.2. Hydration State and Formation Conditions of Calcium Sulfates

Analysis of all the calcium-sulfate-bearing observations reveals that a significant majority appear hydrated (Table 1), indicating either bassanite or gypsum, with anhydrite present in much fewer occurrences. Gypsum has been strongly inferred from Mastcam observations [*Vaniman et al.*, 2013; *Rice et al.*, 2013]. These three phases form and behave differently depending on environmental conditions. Their identification suggests a complex history involving burial and exhumation, variations in temperature, water/rock ratio, and/or chemistry.

Formation of hydrated calcium sulfate phases such as gypsum suggests a precipitation at relative low-temperature conditions, typically below 50°C [e.g., *Hardie*, 1967; *Warren*, 1999]. The persistence of gypsum suggests that conditions did not reach 50°C after those veins formed. The simultaneous formation of gypsum with bassanite is possible because the latter has been identified as a precursor for gypsum. Bassanite or gypsum also could have formed from anhydrite from fluid circulation in late diagenetic stages. In this case, the texture may not correspond to typical gypsum texture (such as fibrous gypsum) but could have preserved the texture of anhydrite [e.g., *Warren*, 1999].

The formation of anhydrite usually requires temperatures higher than 50° when formed as primary precipitates [e.g., *Hardie*, 1967; *Warren*, 1999]. On Earth, anhydrite can form at or close to the surface from enhanced temperatures in sabkha conditions [*Warren*, 1999]. Nevertheless, subsurface conditions and/or the presence of other salts can also lead to anhydrite formation at more ambient temperatures, down to 20°C [*Warren*, 1989], and these conditions are not well known under thermodynamical conditions distinct from usual terrestrial conditions in which those precipitates are found. On Earth, nodular anhydrite is often found in gypsum-rich evaporitic layers buried at depth [e.g., *Shearman*, 1985]. Nodular texture is thus usually considered as secondary, formed by solution-reprecipitation of gypsum to anhydrite. Dehydration, cementation, and compaction are the main drivers of these processes, thus limiting the implications in terms of temperature of the presence of anhydrite [e.g., *Hussain and Warren*, 1989; *Warren*, 1989]. Complex evolution due to multiple episodes of either temperature variations or salinity variations induces complex assemblages and textures linked to multiple transformations between gypsum and anhydrite [e.g., *Testa and Lugli*, 2000; *Paz and Rossetti*, 2006].

Calcium sulfates on Earth are usually strongly modified at exhumation under ambient conditions [*Warren*, 1989]. Similar modifications may occur on Mars, though with perhaps limited rehydration given the lack of liquid water at the present surface. Experimental data have shown that bassanite is the most stable of the three phases under the current Martian atmospheric conditions at low latitudes [*Vaniman et al*., 2009; *Harrison*, 2012]. Rehydration studies showed that bassanite can form from anhydrite even under very low relative humidity conditions and low temperatures [*Robertson and Bish*, 2013]. This may explain why anhydrite was not frequently encountered at YB with the exception of freshly exposed veins in the drill hole and within one depth profile. It also suggests that some of the hydrated calcium sulfates observed by ChemCam could reflect the rehydration of anhydrite exposed at the surface. In contrast, rehydration of anhydrite to gypsum from water vapor alone is unlikely except with very high humidity such as in contact with snow [*Robertson and Bish*, 2013]. Concerning the dehydration of gypsum into bassanite, this process is observed on Earth depending on conditions. Experimental data under Martian conditions show that dehydration of gypsum to bassanite is possible but does not necessarily occur if temperatures remain cold enough [*Robertson and Bish*, 2013]. So the persistence of gypsum at the present surface is possible, whereas its formation from rehydration is less likely. This suggests that gypsum was emplaced during diagenesis, from primary precipitation or by rehydration of anhydrite during late-stages fluid circulation, but not by rehydration in the current environment.

The following scenario provides one possible explanation for the variety of different phases present in the Yellowknife Bay region:

1. Sulfate-saturated pore fluids from an evaporitic layer may have supplied the fluid overpressure necessary for hydraulic fracturing and fluids able to precipitate gypsum within the resultant voids. In this scenario, the environments conducive to initial gypsum deposition and remobilization to filled fractures need to be discussed more in details (see section 5.3).
2. Calcium sulfates with nodular "chicken-wire" texture (e.g., Selwyn) may have occurred as a relatively early diagenetic episode from an early stage in the fluid circulation. The limitation in Selwyn-like texture number at Sheepbed and their lack in the units above the Sheepbed-Gillespie contact suggest that this initial phase was restricted in duration or extent.
3. The main precipitation phase into the fractures emplaced gypsum (and bassanite) as a late-stage diagenetic episode, under conditions that did not lead toward nodular textures.
4. Exhumation at the surface only slightly modified the initial minerals, such as dehydrating locally gypsum into bassanite or rehydrating nodular texture into bassanite.

5.3. Origin of Sulfur-Rich Fluids in the Context of Yellowknife Bay and Gale Crater

Minor elements can be used to define details of the chemistry of fluids. In sulfate minerals, Sr can replace Ca in the calcium sulfate lattices [e.g., *Kushnir*, 1980; *Warren*, 1999]. Salinity is the main factor controlling the strontium co-precipitation in gypsum facies, and thus, it could be used as a salinity indicator. In contrast, the effect of temperature on Sr replacement in gypsum was discarded by experimental tests [*Rosell et al*., 1998], and so any high Sr in the veins is unlikely to be related to enhanced temperatures. The proportion of Sr suggested by the spectra is between 300 and 400 ppm. These values are below those reached by fluids on Earth (500 to 2500 ppm for Sr in Messinian deposits; see review in *Rosell et al*., [1998]), possibly suggesting that the salinity in the Martian fluids may not have been high. Nevertheless, Martian alteration pathways may vary a bit from usual terrestrial ones [*Tosca et al*., 2008], and the signature of Sr may not be that straightforward.

Ba and Zn are other possible tracers of fluid circulation and especially hydrothermal waters [e.g., *Warren*, 1999]. However, the lack of these elements in the ChemCam spectra does not suggest such a possibility, assuming that the nondetection of these elements is not related to limitations from the ChemCam instrument. More work is needed in future studies to refine the abundance and the role of these elements.

Minor elements and hydration levels suggest that burial was limited ($<$3 km) and temperatures were modest ($<$60°C), despite that these conditions would already invoke strong changes from past ambient conditions. Using a thermochemical model based on Gale crater rock and soil compositions, *Bridges et al*. [2013] suggest that the Sheepbed mudstone, of an originally Fe-rich basaltic composition, underwent diagenesis at ~50°C leading to its saponite-rich mineralogy [*Vaniman et al*., 2013]. Pore fluid subsequently evaporated, creating a

sulfate-rich layer [*Bridges et al*., 2013]. Dissolution of this layer led to the precipitation of the nearly pure sulfate veins seen in the Sheepbed member, perhaps also associated with the alteration of other phases leading to the hollow nodules that are also observed in the mudstone [*Grotzinger et al*., 2013]. Such a process is consistent with some of the observations developed in our study but is not fully constrained. For example, there is no direct evidence of evaporitic layers above the Sheepbed member. The Selwyn nodular anhydrite is a singular occurrence and does not point toward an extensive early source of sulfates at the Sheepbed-Gillespie contact. Furthermore, the number of sulfate occurrences seems to decrease from the bottom of the YB formation (Sheepbed member) to the top (Shaler outcrop). Finally, Sheepbed bulk rock compositions do not point toward any enrichment in sulfur that would be related to the natural migration of evaporitic fluids through pore networks, driven by seepage reflux [e.g. *Adams and Rhodes*, 1960] from overlying evaporite facies. In contrast, observations point toward an enrichment in sulfates after cementation of these units. Initial sulfate deposits may have been more prevalent in stratigraphic units that underlie the Sheepbed mudstone, such as a currently nonexhumed evaporate layers, or strata that may have overlain the YB formation but since been eroded away, or a distinctly different unit such as the basal strata of Mount Sharp.

Indeed, Compact Reconnaissance Imaging Spectrometer (CRISM) data point toward the presence of sulfates, locally associated with clays, at the base of Mount Sharp [*Milliken et al*., 2010]. Signatures are relatively weak, rendering difficult the detection of the sulfate species. Spectra of these sulfates are inconsistent with Ca varieties and lack strong Fe absorptions, suggesting they are likely Mg sulfates [*Milliken et al*., 2010]. Nevertheless, bassanite has a much reduced spectral features (compared to gypsum), and accordingly, bassanite could be part of the general polyhydrated sulfates observed there. Also, anhydrite could be present and simply not detected due to the absence of water in its mineral structure. However, if ancient waters once coursed through Mount Sharp, it is possible they could have dissolved some of these sulfate evaporites and transported them down gradient to the lower topographic level of YB. However, stratigraphical relationships remain actually unclear at present, and this question goes beyond the aim of the present study.

5.4. Implications for Sulfates on Mars and for the Habitability of Gale Crater

Sulfates were found by the Opportunity rover at Meridiani Planum [*Squyres et al*., 2004] and in various equatorial regions by the Observatoire pour la Minéralogie, l'Eau, les Glaces et l'Activité (OMEGA) and CRISM spectrometers [e.g., *Gendrin et al*., 2005; *Mangold et al*., 2008; *Massé et al*., 2008]. These sulfate phases appear to be dominated by Mg sulfates, such as the monohydrated mineral kieserite. Clear calcium sulfate signatures were only locally detected: gypsum was detected in the dunes around the Martian north pole and locally in chaotic terrains [*Langevin et al*., 2013; *Massé et al*., 2008]; bassanite has been detected along thin outcrops interpreted to be linked with recent volcanism in Noctis Labyrinthus [*Mangold et al*., 2010]. Infrared spectra and in situ analyses suggested that sulfates on Mars were predominantly dominated by Mg-Fe sulfates, including jarosite, and that this predominance has been inferred to represent predominantly acidic conditions in a progressively more arid environment [e.g., *Squyres et al*., 2004; *Bibring et al*., 2006]. Nevertheless, after reaching a contact with older terrains at Endeavour crater, the Opportunity rover found sulfate veins that were likely gypsum at the location Homestake on Cape York [*Squyres et al*., 2012]. The APXS investigations determined that the Homestake veins had a composition consistent with nearly pure $CaSO_4$, while Pancam multispectral data indicated that these materials were consistent with gypsum rather than anhydrite or bassanite. The gypsum is interpreted to have precipitated from low-temperature aqueous fluids flowing upward from the ancient materials of the rim, leading temporarily to potentially habitable conditions [*Squyres et al*., 2012]. The presence in the Homestake vein of textures consistent with fibrous crystal growth perpendicular to the inferred fracture walls (at Homestake, the vein is sitting in erosional relief above the host material) suggests antitaxial growth within closed fractures under substantial lithostatic pressure. The presence of veins at Gale crater does not contain evidence of antitaxial crystal growth, within limitations of available image resolutions. If confirmed, this would suggest that despite similar depositional processes at Gale and Endeavor craters, that filling of fracture networks at Gale may represent a more near-surface environment.

Gypsum is a mineral of special interest to astrobiology, as gypsum can provide a habitable environment as well as conditions conducive to microbial preservation. For example, studies of the Haughton impact crater on Devon Island, Canada, show microbial colonization of impact-generated selenite (a particularly clear form of gypsum) [*Parnell et al*., 2004]. There, several genera of endolithic cyanobacteria live within cleavage planes of the selenite. While the Haughton selenite is a hydrothermal deposit, it is thought to have formed in the

final stages of hydrothermal activity and is considered to be a low-temperature precipitate. The microorganisms living in the selenite obtain water from moisture that collects in cavities in the cleavage surfaces, and they obtain energy for photosynthesis from light that penetrates the clear crystals. Examples of other microbial gypsum endoliths also have been reported from soils and crusts in a variety of settings, including deserts such as the Atacama [*Dong et al*., 2007], the Arctic [*Ziolowski et al*., 2013], and the Antarctic [*Hughes and Lawley*, 2003]. Microbial dissolution of gypsum has the potential to release calcium and that, in turn, could enhance formation of calcium-rich brines. Through freezing point depression, such brines could extend times of stability of liquid water, enhancing habitability in a freezing, low-water environment, such as might occur on Mars. On Mars, cleavage surfaces could additionally provide protection to organisms from strong winds, freezing temperatures, desiccation, and radiation.

Gypsum additionally is a mineral in which biosignatures can be preserved. Gypsum-permineralized microfossils have been reported from deposits varying in age from ~260 Ma to recent [*Schopf et al*., 2012]; these microfossils have been compared to modern anaerobic, nonphotosynthetic, sulfur-metabolizing microorganisms. In addition, gypsum-preserved stromatolites (macroscopic and laminated, organo-sedimentary structures produced by microbial mats) have been reported from ~0.6 Ma evaporitic deposits [*Allwood et al*., 2013]. Therefore, given its potential for both habitability and preservation, the occurrence of calcium sulfates is an additional interest for the overall habitability and preservation of organics at Yellowknife Bay as interpreted from the Curiosity rover [*Grotzinger et al*., 2013; *Ming et al*., 2014].

6. Conclusion

The Curiosity rover performed detailed analyses of light-toned fractured fills Yellowknife Bay sedimentary deposits. The ChemCam, Mastcam, APXS, and CheMin instruments were able to demonstrate that these fracture fills consist of calcium sulfate veins, for most of them hydrated, signifying gypsum and bassanite. Anhydrite is locally present and is present in a level characterized by a nodular texture. Recent rehydration under present-day conditions may have occurred as well. An intricate assemblage of veins crossed the sediments and precipitation from fluid circulation formed inside the fractures. The presence of veins in the entire ~5 m stack suggests that this process occurred well after sedimentation and partial cementation of those sediments. The origin of the sulfur-rich fluids having led to sulfate precipitations may take place inside previously precipitated sulfate-rich layers, either before the deposition of the Sheepbed mudstones or from unrelated units such as the sulfates at the base of Mount Sharp. The development of these veins after the episodes of deposition of fluvial sediments at the surface indicates a prolonged activity of aqueous processes in relatively nonacidic conditions and under limited temperatures and lithostatic pressures.

Acknowledgments

We acknowledge P. Sobron and an anonymous reviewer for their revisions. Funding in the USA was provided by the NASA Mars Program Office to the MSL project. Funding in France was provided by the Centre National d'Etudes Spatiales (CNES), the Institut National des Sciences de l'Univers (INSU), the Centre National de la Recherche Scientifique (CNRS), and the Observatoire des Sciences de l'Univers Nantes Atlantique (OSUNA). Data used in this study are available at the Planetary Data System (https://pds.jpl.nasa.gov).

References

Adams, J. E., and M. L. Rhodes (1960), Dolomitization by seepage refluxion, *Am. Assoc. Petrol. Geol. Bull.*, *44*(12).

Allwood, A. C., I. W. Burch, J. M. Rouchy, and M. Coleman (2013), Morphological biosignatures in gypsum: Diverse formation processes of Messinian (~6.0 Ma) gypsum stromatolites, *Astrobiology*, *13*(9), 870–886.

Ball, A. J., V. Hohreiter, and D. W. Hahn (2005), Hydrogen leak detection using laser-induced breakdown spectroscopy, *Appl. Spectrosc.*, *59*, 348–353.

Bell J. F. III, et al. (2013), Initial multispectral imaging results from the Mars Science Laboratory Mastcam investigation at the Gale crater field site. Lunar Planetary Science Conf., Abstract N°1417.

Bibring, J.-P., et al. (2006), Global mineralogical and aqueous Mars history derived from OMEGA/Mars express data, *Science*, *312*(5772), 400–404, doi:10.1126/science.1122659.

Bons P. D. (2000), The formation of veins and their microstructures, in *Stress, Strain and Structure—A Volume in Honour of W.D. Means*, vol. 2, edited by M. W. Jessell and J. L. Urai, p. 12, VirtualExplorer.

Bridges, J. C., S. P. Schwenzer, G. Berger, N. Mangold, R. C. Wiens, F. W. Westall, D. Z. Oehler, R. Leveille, and the MSL Science Team (2013), Modelling fluids associated with sulfate veining in Yellowknife Bay, in *Gale Crater*, European Planetary Science Congress, London, U. K.

Clark R. N., G. A. Swayze, R. Wise, K. E. Livo, T. M. Hoefen, R. F. Kokaly, and S. J. Sutley (2007), USGS Digital Spectral Library splib06a, U.S. Geological Survey, Data Series 231, 2007.

Clegg, S. M., R. C. Wiens, J. E. Barefield, E. Sklute, and M. D. Dyar (2009), Quantitative remote laser induced breakdown spectroscopy by multivariate analysis, *Spectrochim. Acta*, *B64*, 79–88.

Clegg S. M., et al. (2013), High calcium phase observations at Rocknest with ChemCam, 44th Lunar and Planetary Science Conference, LPI Contribution No. 1719, p. 2087.

Cosgrove, J. W. (2001), Hydraulic fracturing during the formation and deformation of a basin: A factor in the dewatering of low-permeability sediments, *Am. Assoc. Pet. Geol. Bull.*, *85*, 737–748.

Cousin, A., O. Forni, S. Maurice, O. Gasnault, C. Fabre, V. Sautter, R. C. Wiens, and J. Mazoyer (2011), Laser induced breakdown spectroscopy library for the Martian environment, *Spectrochim. Acta Part B*, *66*, 805–814, doi:10.1016/j.sab.2011.10.004.

Cremers, D. A., and L. J. Radziemski (2006), *Handbook of Laser-Induced Breakdown Spectroscopy*, John Wiley, Chichester, England, doi:10.1002/0470093013.fmatter/pdf.

Dong, G., G. Morrison, and S. Jaireth (1995), Quartz textures in epithermal veins, Queensland—Classification, origin, and implications, *Econ. Geol.*, *90*, 1841–1856.
Dong, H., J. A. Rech, H. Jiang, H. Sun, and B. J. Buck (2007), Endolithic cyanobacteria in soil gypsum: Occurrences in Atacama (Chile), Mojave (United States), and Al-Jafk Basin (Jordan) deserts, *J. Geophys. Res.*, *112*, G02030, doi:10.1029/2006JG00038.
Dudragne, L., P. Adam, and J. Amouroux (1998), Time-resolved laser-induced breakdown spectroscopy: Application for qualitative and quantitative detection of fluorine, chlorine, sulfur, and carbon in air, *Appl. Spectrosc.*, *52*, 1321–1327.
Durney, D. W., and J. G. Ramsay (1973), Incremental strains measured by syntectonic crystal growths, in *Gravity and Tectonics*, edited by K. A. De Jong and R. Scholten, pp. 67–96, Wiley, New York.
Dyar, M. D., J. M. Tucker, S. Humphries, S. M. Clegg, R. C. Wiens, and M. D. Lane (2011), Strategies for Mars remote Laser-Induced Breakdown Spectroscopy analysis of sulfur in geological samples, *Spectrochim. Acta Part B*, *66*, 39–56.
Edgar L., et al. (2013), Cross-stratified facies observed by the Mars Science Laboratory rover at Gale crater, Mars, EGU Vienna, April 2013, EGU2013-14031.
Fabre, C., S. Maurice, A. Cousin, R. C. Wiens, O. Forni, V. Sautter, and D. Guillaume (2011), Onboard calibration igneous targets for the Mars Science Laboratory Curiosity rover and the Chemistry Camera laser induced breakdown spectroscopy instrument, *Spectrochim. Acta B*, *66*, 280–289, doi:10.1016/j.sab.2011.03.012.
Forni O., et al. (2014), First fluorine detection on Mars with ChemCam on-board MSL, LPSC Abstract 1328.
Gendrin, A., et al. (2005), Sulfates on Martian layered terrains: The OMEGA/Mars Express View, *Science*, *307*, 1587, doi:10.1126/science.1109087.
Gottfried, J. L., F. C. De Lucia, and A. M. Miziolek (2009), Discrimination of explosive residues on organic and inorganic substrates using laser-induced breakdown spectroscopy, *J. Anal. At. Spectrom.*, *24*, 288–296, doi:10.1039/b818481j.
Graff T. G., R. V. Morris, S. M. Clegg, R. C. Wiens, and R. B. Anderson (2011), Dust removal on Mars using laser-induced breakdown spectroscopy, Lunar Planet. Sci. LXII, 1916.
Grotzinger, J. P., et al. (2013), A habitable fluvio-lacustrine environment at Yellowknife Bay Gale crater, Mars, *Science*, *434*, doi:10.1126/science.1242777.
Gustavson, T. C., S. D. Hovorka, and A. R. Dutton (1994), Origin of satin spar veins in evaporite basins, *J. Sediment. Res.*, *A64*, 88–94.
Hardie, L. A. (1967), The gypsum-anhydrite equilibrium at one atmosphere pressure, *Am. Mineral.*, *52*, 171–201.
Harrison, T. (2012), Experimental VNIR reflectance spectroscopy of gypsum dehydration: Investigating the gypsum to bassanite transition, *Am. Mineral.*, *97*, 598–609.
Hughes, K. A., and B. Lawley (2003), A novel Antarctic endolithic community within gypsum crusts, *Environ. Microbiol.*, *5*(7), 555–565.
Hussain, M., and J. K. Warren (1989), Nodular and enterolithic gypsum: The "sabkha-tization" of Salt Flat playa, west Texas, *Sediment. Geol.*, *63*, 13–24.
Johnson, J. R., et al. (2014), ChemCam passive reflectance spectroscopy of surface materials at the Curiosity landing site, Mars, *Icarus*, doi:10.1016/j.icarus.2014.02.028.
Kerr, S. D., and A. Thompson (1963), Origin of nodular and bedded anhydrite in Permian shelf sediments, Texas and New Mexico, *Am. Assoc. Petrol. Geol. Bull.*, *47*, 1726–1732.
Kushnir, J. (1980), The coprecipitation of strontium, magnesium sodium, potassium and chloride ions with gypsum: An experiment study, *Geochim. Cosmochim. Acta*, *44*, 1471–1482.
Langevin, Y., F. Poulet, J.-P. Bibring, and B. Gondet (2005), Sulfates in the North Polar region of Mars detected by OMEGA/Mars Express, *Science*, *307*(5715), 1584–1586, doi:10.1126/science.1109091.
Le Mouélic, S., et al. (2014), The ChemCam Remote Micro-Imager at Gale crater: Review of the first year of operations on Mars, *Icarus*, doi:10.1016/j.icarus.2014.05.030.
Mangold, N., A. Gendrin, B. Gondet, S. Le Mouélic, C. Quantin, V. Ansan, J.-P. Bibring, Y. Langevin, P. Masson, and G. Neukum (2008), Spectral and geological study of the sulfate rich region of West Candor Chasma, Mars, *Icarus*, *194*(2), 519–543.
Mangold, N., L. Roach, R. Milliken, S. Le Mouélic, V. Ansan, J. P. Bibring, P. Masson, J. F. Mustard, S. Murchie, and G. Neukum (2010), A Late Amazonian alteration layer related to local volcanism on Mars, *Icarus*, *207*, 265–276.
Massé, M., S. Le Mouélic, O. Bourgeois, J.-P. Combe, L. Le Deit, C. Sotin, J.-P. Bibring, B. Gondet, and Y. Langevin (2008), Mineralogical composition, structure, morphology, and geological history of Aram Chaos crater fill on Mars derived from OMEGA Mars Express data, *J. Geophys. Res.*, *113*(E12), doi:10.1029/2008JE003131.
Maurice, S., et al. (2012), The ChemCam instrument suite on the Mars Science Laboratory (MSL) rover: Science objectives and mast unit description, *Space Sci. Rev.*, *170*, 95–166, doi:10.1007/s11214-012-9912-2.
McLennan, S. M., et al. (2013), Elemental geochemistry of sedimentary rocks in Yellowknife Bay, Gale crater, Mars, *Science*, *343*(6169), doi:10.1126/science.1244734.
Meslin, P.-Y., et al. (2013), Soil diversity and hydration as observed by ChemCam at Gale crater, Mars, *Science*, *341*, doi:10.1126/science.1238670.
Milliken, R. E., J. P. Grotzinger, and B. J. Thomson (2010), Paleoclimate of Mars as captured by the stratigraphic record in Gale crater, *Geophys. Res. Lett.*, *37*, L04201, doi:10.1029/2009GL041870.
Ming, D. W., et al. (2014), Volatile and organic compositions of sedimentary rocks in Yellowknife Bay, Gale Crater, Mars, *Science*, *343*(6169), doi:10.1126/science.1245267.
Nachon, M., et al. (2013), *Sulfate calcium veins observed by the ChemCam instrument onboard Curiosity*, vol. 8, European Planetary Science Congress, London, U. K.
Nanfito A. F. (2008), Timing of diagenesis and deformation of carboniferous gypsum & anhydrites in Spitsbergen, Department Of Geology—Geography University Of Nebaska, Omaha, Bachelor thesis. [Available at maps.unomaha.edu/maher/theses/Nanfitothesis.pdf.]
Ollila A. M., J. G. Blank, R. C. Wiens, J. Lasue, H. E. Newsom, S. M. Clegg, A. Cousin, and S. Maurice (2011) Preliminary results on the capabilities of the ChemCam laser-induced breakdown spectroscopy (LIBS) instrument to detect carbon on Mars. 42nd Lunar & Planetary Science Conference, Houston, Tex., #2395.
Ollila A. M., et al. (2013) Trace element geochemistry (Li, Ba, Sr, and Rb) using Curiosity's ChemCam: Early results for Gale crater from Bradbury Landing Site to Rocknest. LPSC.
Osborne, M. J., and R. E. Swarbrick (1997), Mechanisms for generating overpressure in sedimentary basins: A reevaluation, *Am. Assoc. Pet. Geol. Bull.*, *81*, 1023–1041.
Parnell J., P. Lee, C. S. Cockell, and G. R. Osinski (2004), Microbial colonization in impact-generated hydrothermal sulphate deposits, Haughton impact structure, and implications for sulphates on Mars. *Intl. J. Astrobiol.*, 0(0), 1–10. doi:10.1017/S1473550404001995.
Paz, J. D. S., and D. F. Rossetti (2006), Petrography of gypsum-bearing facies of the Codó Formation (Late Aptian), Northern Brazil, *An. Acad. Bras. Cienc.*, *78*(3), 557–572.
Philipp, S. L. (2008), Geometry and formation of gypsum veins in mudstones at Watchet, Somerset, SW England, *Geol. Mag.*, *145*, 831–844.

Rice M. S., J. F. Bell, A. Godber, D. Wellington, A. A. Fraeman, J. R. Johnson, K. M. Kinch, M. C. Malin, and J. P. Grotzinger, 2013, *Mastcam Multispectral Imaging Results From the Mars Science Laboratory Investigation in Yellowknife Bay*, vol. 8, p. 762, EPSC, London, U. K.
Richardson, W. A. (1920), The fibrous gypsum of Nottinghamshire, *Min. Mag.*, *91*, 77–95.
Robertson, K., and D. Bish (2013), Constraints on the distribution of $CaSO_4 \cdot nH_2O$ phases on Mars and implications for their contribution to the hydrological cycle, *Icarus*, *223*(1), 407–417.
Rosell, L., C. F. Orti, A. Kasprzyk, E. Playa, and T. Peryt (1998), Strontium geochemistry of Miocene primary gypsum: Messinian of southeastern Spain and Sicily and Badenian of Poland, *J. Sediment. Res.*, *68/1*, 63–79.
Sallé, B., J.-L. Lacour, E. Vors, P. Fichet, S. Maurice, D. A. Cremers, and R. C. Wiens (2004), Laser-induced breakdown spectroscopy for Mars surface analysis: Capabilities at standoff distances and detection of chlorine and sulfur elements, *Spectrochim. Acta, Part B*, *59*, 1413–1422.
Schopf, J. W., J. D. Farmer, I. S. Foster, A. B. Kudryavtsev, V. A. Gallardo, and C. Espinoza (2012), Gypsum-permineralized microfossils and their relevance to the search for life on Mars, *Astrobiology*, *12*(7), 619–633.
Schreiber, B. C., and M. El Tabakh (2000), Deposition and early alteration of evaporates, *Sedimentology*, *47*, 215–238.
Schröder S., et al. (2013), First analysis of hydrogen in ChemCam spectra at Curiosity landing site, EGU Vienna, April 2013, EGU2013-11793.
Shearman, D. J. (1985), Syndepositional and late diagenetic alteration of primary gypsum to anhydrite, in *6th Int. Symposium on Salt*, vol. 1, edited by B. C. Schreiber and L. Harner, pp. 41–50, Salt Institute.
Shearman, D. J., G. Mossop, H. Dunsmore, and H. Martin (1972), Origin of gypsum veins by hydraulic fracturing, *Trans. Inst. Min. Metall.*, *81*, B149–B155.
Siebach K., J. Grotzinger, and the MSL Science Team (2013), Raised ridges in the Sheepbed member as evidence for early subaqueous diagenesis at Yellowknife Bay, Gale crater, Mars, AGU abstract.
Sobron, P., and A. Wang (2011), A planetary environment and analysis chamber (PEACh) for coordinated Raman-LIBS-IR measurements under planetary surfaces environmental conditions, *J. Raman Spectrosc.*, doi:10.1002/jrs.3017.
Sobron, P., A. Wang, and F. Sobron (2012), Extraction of compositional and hydration information of sulfates from laser-induced plasma spectra recorded under Mars atmospheric conditions—Implications for ChemCam investigations on Curiosity rover, *Spectrochim. Acta Part B*, *68*, 1–16.
Squyres, S. W., et al. (2004), The Opportunity rover's Athena Science inverstigation at Meridiani Planum, Mars, *Science*, *306*(5702), 1698–1703, doi:10.1126/science.1106171.
Squyres, S. W., et al. (2012), Ancient impact and aqueous processes at Endeavour crater, Mars, *Science*, *336*(6081), 570–576, doi:10.1126/science.1220476.
Stack, K., et al. (2013), An overview of past depositional environments explored by the Curiosity rover at Bradbury Landing and Yellowknife Bay, Gale crater, Mars, *GSA*, *45*(7), 38.
Testa, G., and S. Lugli (2000), Gypsum–anhydrite transformations in Messinian evaporites of central Tuscany (Italy), *Sediment. Geol.*, *130*, 249–268.
Tosca, N. J., A. H. Knoll, and S. M. McLennan (2008), Water activity and the challenge for life on early Mars, *Science*, *320*, 1204, doi:10.1126/science.1155432.
Turekian, K. K., and J. L. Kulp (1956), The geochemistry of strontium, *Geochim. Cosmochim. Acta*, *10*(5–6), 245–296.
Vaniman D. T., D. L. Bish, and S. J. Chipera (2009), Bassanite on Mars, LPSC Abstract N°1654.
Vaniman D., et al. (2013), Data from the Mars Science Laboratory CheMin XRD/XFR instrument, vol. 15, EGU2013-6272, 2013, EGU General Assembly.
Warren, J. (1999), *Evaporites: Their Evolution and Economics*, Blackwell Science, Oxford, U. K.
Warren, J. K. (1982), The hydrological setting, occurrence and significance of gypsum in late Quaternary salt lakes in South Australia, *Sedimentology*, *29*, 609–627.
Warren, J. K. (1989), *"General Concepts." Evaporite Sedimentology*, pp. 1–37, Prentice-Hall, Englewood Cliffs.
Wiens, R. C., et al. (2012), The ChemCam instrument suite on the Mars Science Laboratory (MSL) rover: Body unit and combined system tests, *Space Sci. Rev.*, *170*, 167–227, doi:10.1007/s11214-012-9902-4.
Wiens, R. C., et al. (2013), Pre-flight calibration and initial data processing for the ChemCam laser-induced breakdown spectroscopy instrument on the Mars Science Laboratory rover, *Spectrochim. Acta B*, *82*, 1–27, doi:10.1016/j.sab.2013.02.003.
Williams, R. M. E., et al. (2013), Martian fluvial conglomerates at Gale crater, *Science*, *340*, 1068–1072.
Ziolowski, L. A., N. C. S. Mykytczuk, C. R. Omelon, H. Johnson, L. G. Whyte, and G. F. Slater (2013), Arctic gypsum endoliths: A biogeochemical characterization of a viable and active microbial community, *Biogeosci. Discuss.*, *10*, 2269–2304, doi:10.5194/bgd-10-2269-2013.